UNIVERSITY OF CALIFORNIA, SAN DIEGO

Experiments on Vortex Symmetrization in Magnetized Electron Plasma Columns

A dissertation submitted in partial satisfaction of the

requirements for the degree Doctor of Philosophy

in Physics

by

Ann C. Cass

Committee in charge:

Professor C. Fred Driscoll, Chair
Professor Patrick H. Diamond
Professor Daniel H. E. Dubin
Professor Asoka Mendis
Professor William R. Young

1998

The dissertation of Ann C. Cass is approved, and it is

acceptable in quality and form for publication on

microfilm:

_____

_____

_____

_____

Chair

University of California, San Diego

1998

This dissertation is dedicated to

Dr. Kevin S. Fine,

my great partner in research and in life,

and to my wonderful family

Tom, Cathy, and Jep Johnson.

No matter how far I go, you always mean home to me.

TABLE OF CONTENTS

LIST OF FIGURES

ACKNOWLEDGEMENTS

I have many people to thank for helping me get through seven years of graduate school and a doctoral thesis.

First, I would like to thank my advisor, Fred Driscoll. Fred has been an avid partner in this quest to understand vortex perturbations, and I have learned so much from working with him. In addition, Fred has truly been a supportive and understanding advisor.

I am very grateful to have worked with researcher Kevin Fine for my whole time in the CamV lab. Kevin did a superb job of designing CamV and was primarily responsible for its construction. I would not have finished this thesis without Kevin's daily encouragement and determination to get me over the "humps" of research. Thanks for helping me achieve my goals.

I owe many thanks to David Schecter and Ilya Lansky, whose eigenmode theory work played a crucial role in helping Fred and me understand the complete mode picture. I thank Ross Spencer and Neal Rasband at Brigham Young, who helped me predict quasimode decay rates. Professor Bill Young provided many fruitful discussions. I'm also grateful to Professor Pat Diamond for sparking my interest in this topic and for his heartening encouragement.

I have really enjoyed being a part of the Non-Neutral research group at UCSD. It has been a great pleasure working with Professors Tom O'Neil and Dan Dubin. I have

VITA

May 22, 1969	Born, Winston-Salem, North Carolina
1991	B.S. Duke University
1991-1992	Teaching Assistant, Department of Physics, University of California, San Diego
1992-1998	Research Assistant, University of California, San Diego
1998	Ph.D., University of California, San Diego

PUBLICATIONS

Fine, K.S., A.C. Cass, W.G. Flynn, and C.F. Driscoll, *Relaxation of 2D Turbulence to Vortex Crystals.* Physical Review Letters, 1995. **75**(18): p. 3277-80.

FIELDS OF STUDY

Major Field: Physics

Studies in Plasma Physics.
Professors Patrick H. Diamond and Thomas M. O'Neil

Studies in Classical Mechanics.
Professors Thomas M. O'Neil and Henry D. Abarbanel

Studies in Electromagnetism.
Professor Herbert Levine

Studies in Quantum Mechanics.
Professor Julius Kuti

Studies in Statistical Mechanics
Professor Daniel H. E. Dubin

Studies in Mathematical Physics
Professor Marshall N. Rosenbluth

ABSTRACT OF THE DISSERTATION

Experiments on Vortex Symmetrization in Magnetized Electron Plasma Columns

by

Ann C. Cass

Doctor of Philosophy in Physics

University of California, San Diego, 1998

Professor C. Fred Driscoll, Chair

Experiments are presented on vortex symmetrization in magnetized electron columns, which follow the same (r, θ) dynamics as two-dimensional, incompressible, inviscid fluids. Fluid vorticity (plasma density) is measured directly using a phosphor screen and CCD camera. The fluid has low dissipation (equivalent $\mathrm{Re} \approx 10^5$) and is contained within free-slip cylindrical walls.

In freely evolving turbulence, a novel state called "vortex crystals" is observed to form. Strong "clumps" of vorticity cease merging and form symmetric arrays within a smooth background of lower vorticity. During vortex crystal "cooling", the measured chaotic vortex motion decreases by at least a factor of 6. The crystal state represents a novel ordered meta-equilibria for near-inviscid 2D fluid turbulence.

Measurements of the symmetrization of initially distorted vortices are also presented. Vorticity perturbations of the form $e^{im\theta}$ are applied to otherwise axisymmetric monotonically decreasing vortices, and are allowed to evolve freely. Essentially, we find that vorticity perturbations persist for long times due to effectively undamped surface waves.

The long-lived waves are generalized versions of the surface waves found by Kelvin for "top-hat" vortex patches. For many smooth vorticity profiles, Kelvin waves propagate unchanged. For vortices with non-zero vorticity at a "critical radius", waves initially decay exponentially (and are properly called "quasimodes"); however, for large amplitude perturbations, linear decay saturates with the formation of Kelvin's "cat's eye" structures.

A new numerical method allows us to predict the frequency and radial mode structure of linear waves on our measured vortices. The calculated modes agree well with experimental measurements. For vortices with damped quasimodes, estimated decay rates agree with measurements to within a factor of 0.4-1.5.

After 5-10 wave periods of exponential decay, vorticity filaments form Kelvin's "cat's eye" structures. Within these "cat's eyes," trapped fluid moves in and out of phase with the wave, modulating the wave amplitude at a "trapping frequency". The measured frequency scales as $f_{to} \propto A_d^{1/2}$, as predicted theoretically. The cat's eye structure is stable, lasting for up to $10^4\,\tau_R$, until the weak plasma dissipation "smears" out the filaments. Thus, despite the inviscid decay process, we find that for damped or undamped Kelvin waves, vortices remain asymmetric on inviscid time scales.

CHAPTER I

INTRODUCTION AND SUMMARY

A. Introduction

Turbulent flows occur in a wide variety of physical systems, ranging from earth's atmosphere to hot fusion plasmas confined in thermonuclear reactors [1, 2]. Although there is no rigorous scientific definition of turbulence, a turbulent flow must exhibit randomness in both space and time, excitations of many degrees of freedom, and extensive mixing of fluid elements. Due to the complexity of the nonlinear interaction, a comprehensive physical picture of turbulence is still elusive, and it remains "the last great unsolved problem of classical physics," as was dubbed by Richard Feynman. Turbulence appears to behave differently from one system to another, depending on the flow dynamics involved, as well as on the initial and boundary conditions. Modern research has concentrated on finding universal properties that can provide a clear physical understanding of the observed phenomena [3].

Under certain conditions, a three-dimensional physical system can be modeled by neglecting one of the spatial degrees of freedom. For example, geophysical phenomena such as mesoscale oceanic and atmospheric flows are approximately two-dimensional (2D), due to the effects of earth's rotation and the relatively small vertical extent of the flows [4]. In addition, the macroscopic behavior of strongly magnetized plasmas is often effectively 2D, due to the "stiffening" effect of the confining magnetic field [5].

Other 2D flows include thin liquid films, cryogenic superfluids, and self-gravitating disk galaxies [6].

Two additional flow properties, low viscosity and incompressibility, are also important characteristics of the flows considered here. Low viscosity means that fine-scale variations in the fluid velocity can evolve and persist without being dissipated by the inherent "friction" between adjacent fluid elements. Many flows are effectively incompressible, meaning that the volume of a fluid element does not change as it moves; water is an incompressible liquid, and many gas flows are approximately incompressible.

The 2D dynamics of incompressible fluids has been studied for over a hundred years [6]. The flows are characterized by the vorticity (i.e., local rotation) of the fluid, and regions of strong vorticity (i.e., vortices) can be long-lived and can strongly affect the flow evolution. In the inviscid limit, a 2D incompressible flow is simply the advection of scalar fluid vorticity; for this reason, 2D turbulence exhibits some intriguing features quite different from its 3D counterpart. For example, as the 2D turbulence evolves, the kinetic energy of the flow tends to condense into large 2D vortices, rather than being transferred to small spatial scales.

Freely evolving 2D turbulence is of particular interest, since the lack of external forcing eliminates unwanted complications. Recently, insights on free relaxation have been obtained through extensive analytical and computational studies, enabled by the availability of high performance computers. Theorists have attempted to predict the relaxed state of turbulence, based on statistical arguments and the quantities known to be conserved by the flow. However, evidence indicates that one must also consider

2

long-lived dynamical structures in order to understand the final state [7].
Unfortunately, laboratory experiments are relatively few [8], because it is difficult to
devise a well-diagnosed, two-dimensional, experimental system with low dissipation.

A magnetically confined pure electron plasma column can be considered as two-
dimensional when the electron axial bounce motion is much faster than the " $\mathbf{E} \times \mathbf{B}$
drift" in the (r, θ) plane perpendicular to the magnetic field. In this regime, the
perpendicular dynamics is governed by the Euler equation for 2D incompressible
inviscid fluids, with the electron density being proportional to the vorticity. Further,
the flow vorticity (i.e., electron density) can be directly measured with high resolution,
allowing detailed quantitative comparisons with theoretical predictions.

These magnetized electron columns provide excellent opportunities to study 2D
near-inviscid fluid dynamics and turbulence. The dissipation time τ_{diss} of vortex
structures is much longer than typical rotation times τ_R, allowing high Reynolds
numbers $\mathrm{Re} \approx \tau_{diss} / \tau_R \approx 10^4 - 10^5$ which are difficult to achieve in ordinary fluids.
For fine spatial scales or long times, plasma "viscous" [9] or diffusive effects [10]
become significant; however these are *not* in general modeled by the Navier-Stokes
equation.

B. Summary

Experimental results are presented on two related topics: the relaxation of
turbulence to novel "vortex crystal" states; and the inviscid decay of vortex surface
waves.

In Chapter III, we describe the novel vortex crystal states, a meta-equilibrium which occurs during the free relaxation of the fluid system from a highly filamented initial vorticity distribution [11]. Two-dimensional turbulence normally relaxes through vortex merger and filamentation, with energy flowing to large scales and enstrophy transferred to fine scales where it is eventually dissipated. Here, electron plasma experiments show that this relaxation can be arrested by spontaneous "cooling" of the chaotic vortex motions, leading to regular lattices of vortices within a uniform background of weaker vorticity.

The vortex crystal states consist of 5-11 individual vortices each with vorticity 4-6 times the background vorticity, arranged in a lattice pattern which rotates with the background. In plasma terms, rods of enhanced electron density ($n \approx 7 \times 10^6 \, \text{cm}^{-3}$) are maintaining self-coherence and positions relative to each other for several seconds, while $\mathbf{E} \times \mathbf{B}$ drifting with a diffuse background ($n_B \approx 2 \times 10^6 \, \text{cm}^{-3}$). Vortex crystal states are repeatedly observed over a range of filament bias voltages, but the characteristics of the initial $n(r, \theta)$ required for these states to form are not yet understood. One important characteristic of the plasma experiments is that there is only one sign of vorticity.

Reduction of the chaotic advective motions, or "cooling" of the individual vortices, is required to form the vortex crystal states. We characterize these vortex motions by the average magnitude of the random velocities of the individual vortices, $|\delta \text{V}|$, relative to the rotating frame in which the mean discrete vortex velocity is zero. The measured $|\delta \text{V}|$ decreases a factor of 6 during the formation of the crystal,

whereas only slight cooling is seen for sequences which evolve to a single, monotonically decreasing vortex.

It appears that the vortex cooling occurs due to an interaction between the individual vortices and the boundary of the background vorticity. In the simplest interaction, the vortices excite small amplitude surface waves on the background, and these waves are damped by spatial Landau damping; in more complicated interactions, nonlinear filaments are observed to form on the surface. These ideas are being pursued theoretically by other researchers.

In Chapter IV, we discuss experiments on the inviscid damping of vorticity waves, a mechanism which may be influential in forming the vortex crystal. We characterize the evolution of inviscid vorticity perturbations varying as $\delta\zeta(r,\theta,t) \propto A(t)\,\xi(r)\sin(m\theta - \omega t)$ on electron columns with sheared azimuthal rotation. Coherent waves of vorticity are readily excited by perturbations distant from the vortex, and we find that these waves ultimately persist for long times, even in cases where resonant processes cause them to partially damp.

Starting with an axisymmetric plasma with vorticity profile $\zeta_0(r)$, we apply voltages on wall sectors to create a $m=2$ vorticity perturbation $\delta\zeta^{(2)}$, which then freely evolves. Most of the perturbation remains coherent and is called the "discrete" Kelvin wave or "diocotron" mode. Theory suggests [12] that the rest of the initial perturbation $\delta\zeta^{(2)}(r)$ can be described as a superposition of "continuum modes" which should then phase mix away. Surprisingly, we observe that almost all of

5

$\delta\zeta^{(2)}(r)$ *is* the discrete mode, with typically 10% residual; this is because external perturbations do not couple strongly to the continuum modes.

The discrete mode may persist for tens of thousands of wave periods, or it may be a "quasimode" which damps due to an inviscid wave-fluid resonance. The measured quasimode frequencies agree with theory predictions at the 10% level. More significantly, the measured initial damping rates agree within a factor of 2 to 5 with the predictions of "spatial Landau damping" [13], numerically calculated from the measured $\zeta_0(r)$.

The damping of even moderately large amplitude waves is strongly affected by nonlinear effects. After exponential damping at early times, the mode amplitude "bounces", then asymptotes to a constant amplitude. Experimental images clearly show that the damping and bounces are due to low density filaments peeling off and eventually forming closed "cat's eye" structures. The measured amplitude-bounce (or "trapping oscillation") frequency f_{to} scales with mode amplitude A as $f_{to} \propto A^{-1/2}$, as expected with the orbits of fluid particles trapped within the cat's eyes.

Finally, we discuss the nonlinear effect of damping which occurs only when the wave is large. This can be understood as the large amplitude wave modifying the symmetric vorticity profile $\zeta_0(r)$, so that the resonant-layer decay can occur. In this case, the damping process results in visually striking filaments outside the vortex.

CHAPTER II

Design and Operation of the CamV Apparatus

A. Overview

The CamV electron apparatus was designed and constructed to create and
magnetically confine electron plasmas, with CCD camera images diagnosing the 2D
(r,θ) flows of electrons across the magnetic field. These flows cause rapid cross-field
transport of particles and energy. The plasmas can be thought of as "rods" of charge,
moving in 2D as an incompressible, inviscid fluid. Thus, they make excellent systems
on which to study 2D inviscid fluid dynamics.
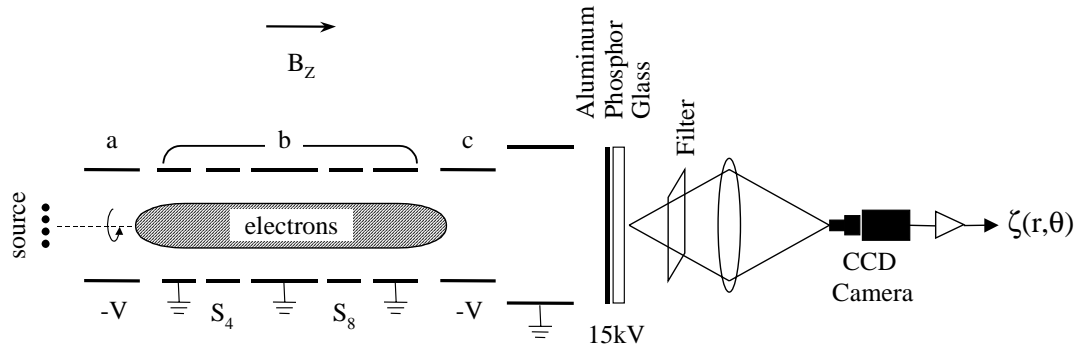
Figure 1. The cylindrical experimental apparatus CamV with phosphor screen/CCD
camera diagnostic.

Figure 1 shows the experimental device with the imaging diagnostic. Electrons
from a spiral tungsten filament are trapped in a series of conducting cylinders with
wall radius $R_W = 3.5$ cm enclosed in a vacuum chamber (with base pressure $P \leq 10^{-9}$
torr). The electrons are contained axially by negative voltages $(-50\,\text{V})$ on the two end
cylinders, and confined radially by a uniform axial magnetic field (typically

$B_z = 4 \, \text{kG}$), resulting in a confinement time of about 100 seconds. The trapped electron column typically has density $n_{3D} \leq 7 \times 10^6 \, \text{cm}^{-3}$, radius $R_v \approx 1.5 \, \text{cm}$, and axial length $L_p \approx 50 \, \text{cm}$. The plasma Debye length is $\lambda_D \geq 3.32 \, \text{mm}$, much smaller than the column dimensions R_v and L_p.

The electrons have average kinetic energy $1/2 m \text{v}_Z^2 = kT \approx 1 \, \text{eV}$ and are effectively collisionless, with collisional mean-free-path $\lambda_{ee} \approx 3 \, \text{km}$ and collision frequency $\upsilon_{ee} = 0.1 \, \text{sec}^{-1}$. Individual electrons bounce rapidly back and forth along the magnetic field, at a rate $f_z \equiv \overline{\text{v}}_Z / 2 L_p \approx 0.4 \, \text{MHz}$, averaging over any z-variations. Kinetic energy perpendicular to B_z is bound up in cyclotron orbits which are fast enough ($f_c \approx 11 \, \text{GHz}$) and small enough ($r_c \approx 5 \mu\text{m}$) so as to be ignorable.

Electric fields cause the electrons to "$\mathbf{E} \times \mathbf{B}$ drift" across the magnetic field as an effectively incompressible fluid. Typical $\mathbf{E} \times \mathbf{B}$ rotation frequency at the center of the plasma is $\Omega_0 / 2\pi = 180 \, \text{kHz}$. The 2D flow velocity $\mathbf{v}(r, \theta)$ flow of the electrons is described by the 2D drift-Poisson equations, and the 2D electron density $n(r, \theta)$ will be seen to be proportional to the flow vorticity $\zeta(r, \theta) = \nabla \times \mathbf{v}(r, \theta) \cdot \hat{\mathbf{z}}$.

At any desired time, the z-integrated electron density $n(r, \theta, t)$ is measured (destructively) by dumping the electrons axially onto a phosphor screen, from which the luminescence is imaged by a low-noise 512×512 pixel CCD camera. The shot-to-shot variations in the initial profiles are small, i.e., $\delta n / n \leq 10^{-2}$, so the time evolution can be inferred from a sequence of shots with differing hold times.
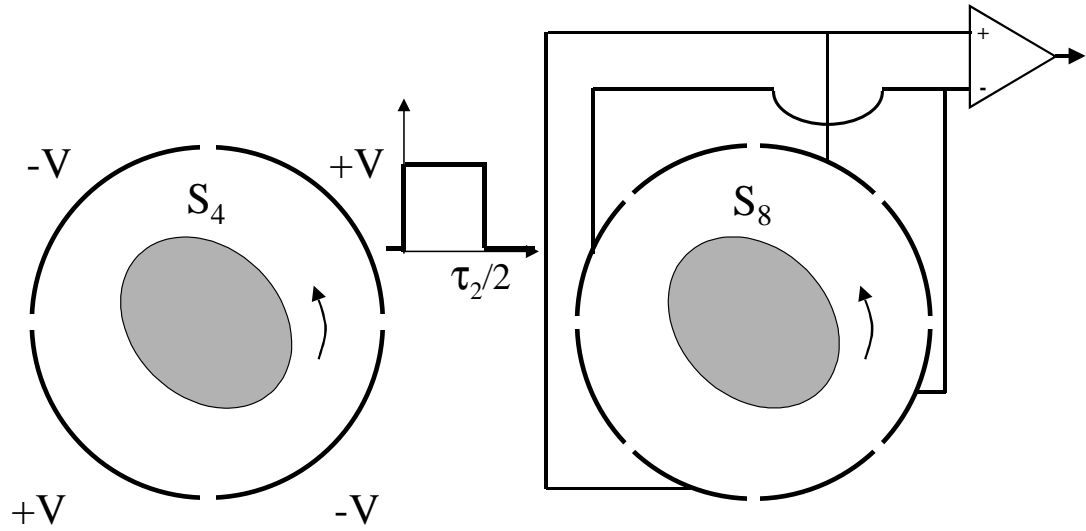
Figure 2. 4-part and 8-part sector probes, together with applied voltages and receiver to launch and detect m=2 perturbations.

B. Description of the Apparatus

The CamV electrode stack has 10 containment cylinders, giving a maximum plasma length of $L_p = 60\,\mathrm{cm}$. Two of the electrodes are divided azimuthally for sending and receiving waves: one electrode has 4 sectors, and the other has 8, as shown in Figure 2. More generally, we are able to displace the column in (r, θ) or compress it axially by applying voltages to the wall sectors, or to full electrodes.

The superconducting magnet has a horizontal room temperature bore 12 3/4 inches in diameter and 68 inches long. Maximum field is 20 kG, constant within $\pm 2\%$ over a length of 120 cm. The magnet enables scaling of electron plasma characteristics over more than 2 decades in field, i.e., 0.1 - 20 kG.

The source of the electrons is a spiral-wound filament of tungsten wire of radius $R_{fil} = 1.2$ cm and resistance $Z_{fil} = 1\,\Omega$, heated with a sinusoidal current I_h at frequency $f_{fil} = 16$ kHz. The ohmic voltage drop across the filament is V_h, where $V_h = I_h Z_{fil}$. The bias voltage at the center of the filament, V_b, is set independently. For the quiescent injection normally used, the plasma is injected when the filament current and voltage is positive, such that the filament voltage $V_{fil}(r)$ closely matches the space charge potential of the plasma, i.e., $V_{fil} = V_b + V_h (r / R_{fil})^2$ [14, 15]. Then V_h determines the local density n_{3D} (number / cm^3) and V_b determines the "line density" of electrons $N_L = \pi R_p^2 n_{3D}$ (number/cm-length). These voltages are chosen to obtain the desired experimental parameters.

Alternatively, the plasma may be injected when the heating voltage is negative, such that $V_{fil} = V_b - |V_h|(r / R_{fil})^2$. Originally, the vortex crystal state discussed in Chapter III was found for only negative heating currents within a small range of bias voltage ($V_b \approx -5 \rightarrow 0\,\text{V}$). Now using a more emissive filament, vortex crystals are obtained for positive and negative filament currents.

The system is operated in an inject/hold/dump cycle. During injection, cylinder a of Figure 1 is grounded and cylinder c is biased negatively; then cylinder a is biased negatively to cut off the incoming electrons and trap electrons within cylinder b. During the hold phase, the trapped electrons may be transported across the field by various processes. A variable time (t) after injection, cylinder c is gated to ground potential, dumping the remaining electrons out that end.

Prior versions of these apparatuses had moveable and fixed collectors to measure the dumped electrons at one or several particular (r,θ) positions. The CamV apparatus uses a phosphor to determine $n(r,\theta)$ for all (r,θ) on a single shot. The entire inject/hold/dump cycle may be repeated up to 100 times per second, although image acquisition requires several seconds.

Figure 1 includes a simplified schematic of this diagnostic system. About 30 cm away from the dump cylinder lies a phosphor screen. The screen consists of a round of quartz glass, 10.2 cm in diameter, coated with blue-green (P22B) phosphor. A thin layer (thickness ≈ 1500 Å) of aluminum over the phosphor blocks the light generated by the hot (1800°K) filament source. At the time of dump, the screen is biased to 15 kV, which axially accelerates the electrons and minimizes the distortions on the 2D density distribution.

The intensity of the luminescence generated by the electron impacts is locally proportional to the number of electrons collected per unit area. The light from the phosphor passes through a vacuum window, and is focused by a 50 mm f 2 lens onto the 512×512 CCD chip of a camera. Two conventional optical filters further reduce the reddish filament light, without degrading the blue-green phosphor light signal.

The phosphor and camera imaging system gives images with high resolution and high dynamic range. Plasmas with density $n_{3D} \approx 10^7 \, \mathrm{cm}^{-3}$ over a column of length 50 cm give 5×10^8 electrons / cm^2 on the phosphor. Since these electrons are accelerated to 15 kV, the phosphor gives off about 400 photons per electron, i.e., 2×10^{11} photons / cm^2 from the phosphor. Taking camera collection efficiency into

account, the CCD receives about 1.3×10^{10} photons / cm^2 from the phosphor, i.e.,

9.1×10^4 photons per pixel onto the 512×512 array imaging a phosphor area of

$7\,\text{cm} \times 7\,\text{cm}$. The CCD has a quantum efficiency of about 8.7% for blue-green

phosphor light, giving 7.9×10^3 electrons/pixel. The CCD digitizer gain is 7.5

electrons/count, so the digitized signal is about 1000 counts per pixel. The aluminum

coating and blue filter reduce the "noise" from stray filament light to about 2 counts:

the blue-green phosphor was chosen to optimize this filtration. Thus, the system can

nominally give a 500:1 signal-to-noise ratio with a spatial resolution of

$2R_W / 512 \approx 0.13$ mm.

The data is digitized to 16 bits by the CCD camera and is stored as a 512×512

array of CCD counts. In order to further remove the pattern of the background light

emitted by our filament, we subtract a "light-zero" from each data image, where the

light-zero is another 512×512 camera image taken when no plasma was present. We

align each image spatially with crosses (called "fiducials") scratched in the Al coating

of the phosphor screen, well outside of the plasma trap wall. Software identifies the

fiducials and shifts the light-zero in x- and y-pixels until it is spatially aligned with the

data image, and then subtracts the light-zero from the data image. In doing this

subtraction, we also adjust for any changes in filament light intensity or camera shutter

speed by applying an overall gain factor to the light-zero so as to minimize the signal

for $r > R_W$ (where there is no plasma).

The calibration from CCD counts to electron density is obtained from a separate

direct electrical measurement of the dumped charge. For this, we use a metal "end"

plate, rotated so as to completely cover the end of the electrode stack. In consecutive shots, we dump the plasma onto the end plate and then onto the phosphor screen. We measure the voltage V_p induced on the collimator plate, separately measure the end plate capacitance to ground, C_p, and thereby get the total charge $Q = C_p V_p$. This gives us a single factor which converts from CCD counts to number of electrons.

C.   2D $\mathbf{E} \times \mathbf{B}$ Drift Dynamics

For plasmas in which the axial bounce frequency is large compared to the azimuthal rotation frequency, low frequency collective phenomena (e.g., "diocotron" modes, turbulence, and vortices) can be described approximately by bounce-averaged $\mathbf{E} \times \mathbf{B}$ drift dynamics. We approximate the 10^9 electrons by a continuous 2D density $n(r,\theta,t)$, with velocity $\mathbf{v}(r,\theta,t)$ arising due to the 2D electrostatic potential $\phi(r,\theta,t)$. This (r,θ) flow is then described by the 2D drift-Poisson equations,

$$
\begin{aligned}
&\nabla_\perp^2 \phi(r,\theta,t) = 4\pi e n \\
&\frac{\partial n(r,\theta,t)}{\partial t} + \mathbf{v} \cdot \nabla_\perp n = 0 \\
&\mathbf{v}(r,\theta,t) = \frac{c}{B} \hat{\mathbf{z}} \times \nabla_\perp \phi .
\end{aligned}
\tag{1}
$$

where $-e$ is the electron charge and c is the speed of light.

The 2D drift-Poisson equations are isomorphic to the Euler equations for the 2D flow of an incompressible and inviscid neutral fluid [12], [16-18]. These equations can be written as

$$\nabla_{\perp}^2 \psi = \zeta$$

$$\frac{\partial \zeta}{\partial t} + \mathbf{v} \cdot \nabla_{\perp} \zeta = 0 \qquad (2)$$

$$\mathbf{v} = \hat{z} \times \nabla_{\perp} \psi,$$

where $\psi(r,\theta,t)$ is the stream function and $\zeta(r,\theta,t) = (\nabla_{\perp} \times \mathbf{v}) \cdot \hat{\mathbf{z}}$ is the z-component of the vorticity. Equations (1) and (2) are identical under the identifications

$$\mathbf{v} \longrightarrow \mathbf{v}$$

$$\psi \longrightarrow \frac{c}{B} \phi \qquad (3)$$

$$\zeta \longrightarrow 4\pi e \frac{c}{B} n$$

The conducting metal walls give boundary condition $E_{\theta}(R_W,\theta) = \partial\phi / \partial\theta \big|_{R_W} = 0$, or $\phi(R_W,\theta) \propto \psi(R_W,\theta) = \text{const}$. At the wall, the tangential velocity $v_{\theta}(R_W,\theta) \propto \partial\phi / \partial r$ is finite, but there are no $\theta-$ forces, giving a true free-slip boundary condition. In the present experiments, there are also typically no electrons (vorticity) near the wall to complicate this boundary condition.

Thus, an initial distribution of electrons $n(r,\theta,t=0)$ in a cylinder will have vorticity $\zeta \propto n$, and will evolve the same as an initial distribution of vorticity ζ in a uniform fluid such as water. (Of course, this is only true to the extent the water dynamics remains 2D in character.) For example, a single column of electrons in our apparatus is equivalent to a finite area vortex in a bucket of water. If the vortex is centered and azimuthally symmetric, it will have a stationary flow field $v_{\theta}(r)$. Outside the region of vorticity, the flow falls off as $v_{\theta} \propto 1/r$. In the electron system, this $1/r$

14

velocity profile arises naturally from Poisson's equation, since $E_r \propto 1/r$ outside the charge column.

One advantage of the electron experiments for testing 2D fluid theory is that the electron system tends to remain 2D due to the magnetic field and the rapid axial bounce motion. Another advantage is that the electron column has low internal viscosity, and no boundary layers at the radial edge or axial end of the system.

Limitations to this isomorphism arise due to the discreteness of the individual electrons, and due to the finite axial length of the confinement system. For fine spatial scales or long times, plasma "viscous" [9] or diffusive effects [10] not contained in Eqns. (2) become significant; however, these are *not* in general modeled by the Navier-Stokes equation. In particular, the effective viscosity of the $\mathbf{E} \times \mathbf{B}$ flow vanishes where the vorticity (i.e*.,* electron density) vanishes. We emphasize, however, that the results presented in this thesis are inviscid effects, occurring on time-scales much less than non-ideal effects.

CHAPTER III

Vortex Crystals

D. Overview

In the free relaxation of turbulence in nearly inviscid 2D flows, energy flows to long wavelengths, while enstrophy is dissipated on fine scales [19]. This leads to inviscid invariants which are "fragile" or "robust" in the presence of weak viscosity [20]. Relaxed states have been predicted based on maximization of entropy [21, 22] or minimization of enstrophy [23, 24]; and surprising agreement with the minimum enstrophy states has been found in experiments in some parameter regimes [25].

However, experiments [7] and computation [26, 27] demonstrate that long-lived nonlinear vortices generally dominate the evolution, arising even from structureless initial conditions. The vortices move chaotically due to mutual advection, resulting in pairwise merger events and the formation of filamentary structures. A scaling theory of "punctuated Hamiltonian" relaxation [28-30] based on point-vortex-like motions punctuated by idealized mergers predicts power law dependences of vortex properties, e.g., the number of vortices $N_v \propto t^{-\xi}$, and simulations have suggested $\xi = 0.75$. Contour dynamics calculations suggest more complicated merger and filamentation events, and give different scaling exponents [31]. Electrolyte experiments with strong dissipation have shown a range of exponents [8, 32].

E. Experiments

Here, we observe the free relaxation of turbulence in magnetized electron columns, which evolve as near-ideal 2D fluids. The initial relaxation is nominally consistent with punctuated Hamiltonian dynamics. However, we find that the relaxation can be arrested by the formation of vortex crystals: for some initial conditions, the chaotic motion of the vortices is "cooled", no further merger events occur, and the vortices form a rigidly rotating lattice within a uniform background of vorticity. The vortex crystal state is observed to persist for up to 10^4 turnover times, until dissipation acts on the individual vortices. Similar geometric patterns of point vortices have been seen in rotating superfluids, where friction arises from interaction with normal fluid [33, 34].

In our case, the cooling appears to be an essentially inviscid 2D fluid process, showing little 3D length dependence, and occurring in a few turnover times. We speculate that the cooling is caused by the interchange of energy between the motion

of individual vortices and the background vorticity, made irreversible by the inevitable fine-scale dissipation or mode damping [12, 35, 36].

For the experiments described here, we initially trap a highly filamented electron density distribution from the spiral electron source, rather than a smooth profile as studied previously [25]. Many individual vortices then form due to local Kelvin-Helmholtz instabilities, and this turbulent state evolves and relaxes by chaotic vortex advection and mergers.
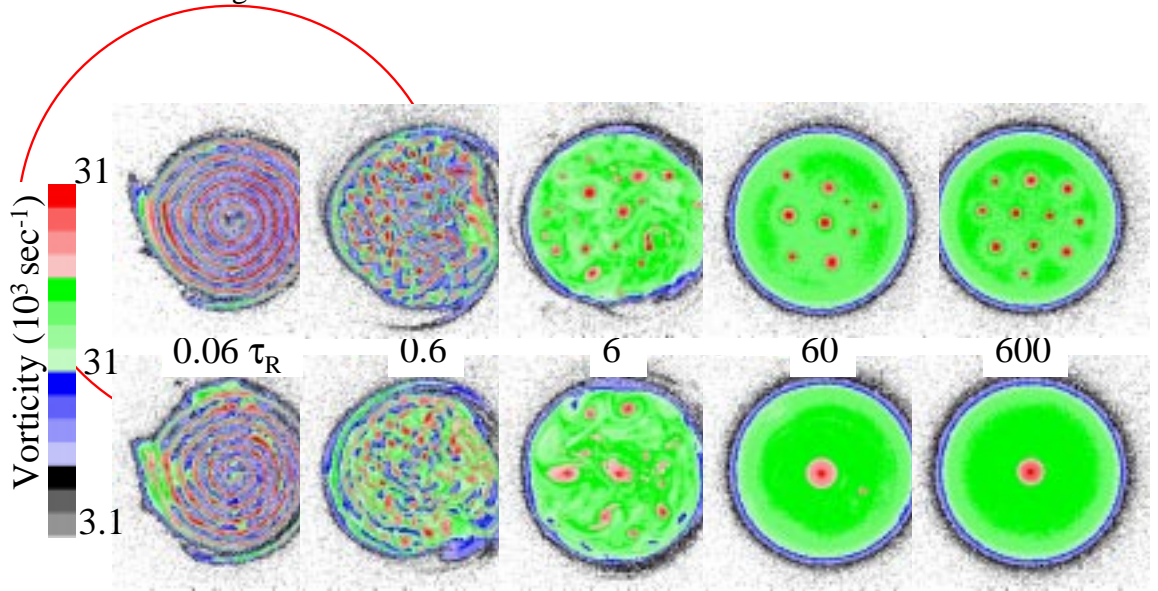
Figure 3. Images of vorticity at five times for two sequences from similar initial conditions. The red arcs indicate the wall radius.

Figure 3 shows the measured vorticity $\zeta(r,\theta,t)$ at five times for two slightly different initial conditions; the two initial conditions are obtained from different filament bias voltages. The upper sequence forms vortex crystals, whereas the lower sequence relaxes rapidly to a monotonically decreasing profile. The vortex crystal states consist of 5 to 11 individual vortices, each with vorticity 4 to 6 times the background vorticity, arranged in a lattice pattern which co-rotates with the background. In plasma terms, rods of enhanced electron density ($n_{3D} \approx 7 \times 10^6 \, \mathrm{cm}^{-3}$) are maintaining self-coherence and positions relative to each other for several seconds, while $\mathbf{E} \times \mathbf{B}$ drifting with a diffuse background ($n_B \approx 2 \times 10^6 \, \mathrm{cm}^{-3}$). Vortex crystal states are repeatedly observed over a range of filament bias voltages, but the characteristics of the initial $n(r,\theta)$ required for these states are not yet understood.
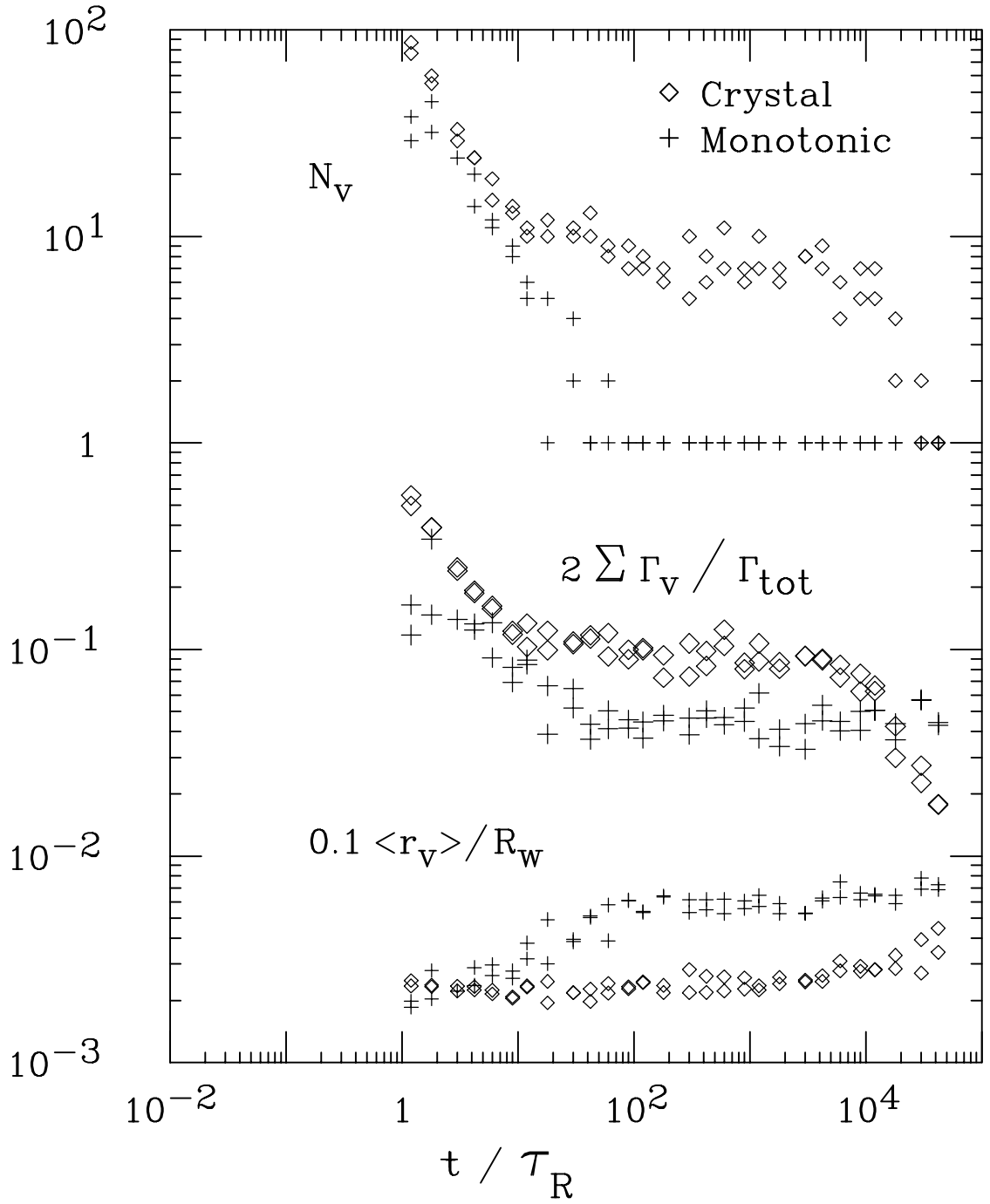
Figure 4. Evolution of the number of vortices N_v, vortex circulation $\sum \Gamma_v$, and average vortex size $\langle r_v \rangle / R_W$ for the two sequences.

Figure 4 shows the number of distinct vortices N_v, the total circulation in these vortices $\sum \Gamma_i$, $i = 1, 2, \ldots N_v$, and the average vortex radius $\langle r_i \rangle$ for the two sequences after distinct vortices form. The vortex counting algorithm is essentially that of McWilliams [37]. We look for simply connected regions of constant vorticity greater than the background vorticity, and count those larger than a minimum threshold. Unlike McWilliams, we do not exclude elongated structures. In both sequences, the unstable filamentary initial condition forms $N_v = 50$ to 100 vortices of roughly equal circulation, after which N_v initially decreases as $N_v \propto t^{-\xi}$, with $\xi \approx 1$. This relaxation is generally consistent with the scaling of Refs. [28, 29]; the observed ξ range from 0.4 to 1.1 as the initial conditions are varied, with 0.8 being commonly observed. Here, the merger, filamentation, and diffusion result in a decrease in the discrete vortex circulation, roughly as $\sum \Gamma_v \propto t^{-0.6}$ in Fig. 4.

In the evolution of the top sequence in Fig. 3, the relaxation is arrested by the "cooling" of the chaotic vortex motions, with formation of vortex crystals by time $10\,\tau_R$, where $\tau_R \approx 170\,\mu s$ is the bulk vortex rotation time. The diamonds in Fig. 4 show that 8 to 10 distinct vortices survive for about $10^4\,\tau_R$. When the surviving vortices all have about the same circulation Γ_v, the patterns are quite regular, as seen at $60\,\tau_R$ in Fig. 3.

Figure 5 shows images of the dissipation of the vortex crystal state at later times. By about $10^4\,\tau_R$, N_v decreases to 1 as the individual vortices decay away in place.
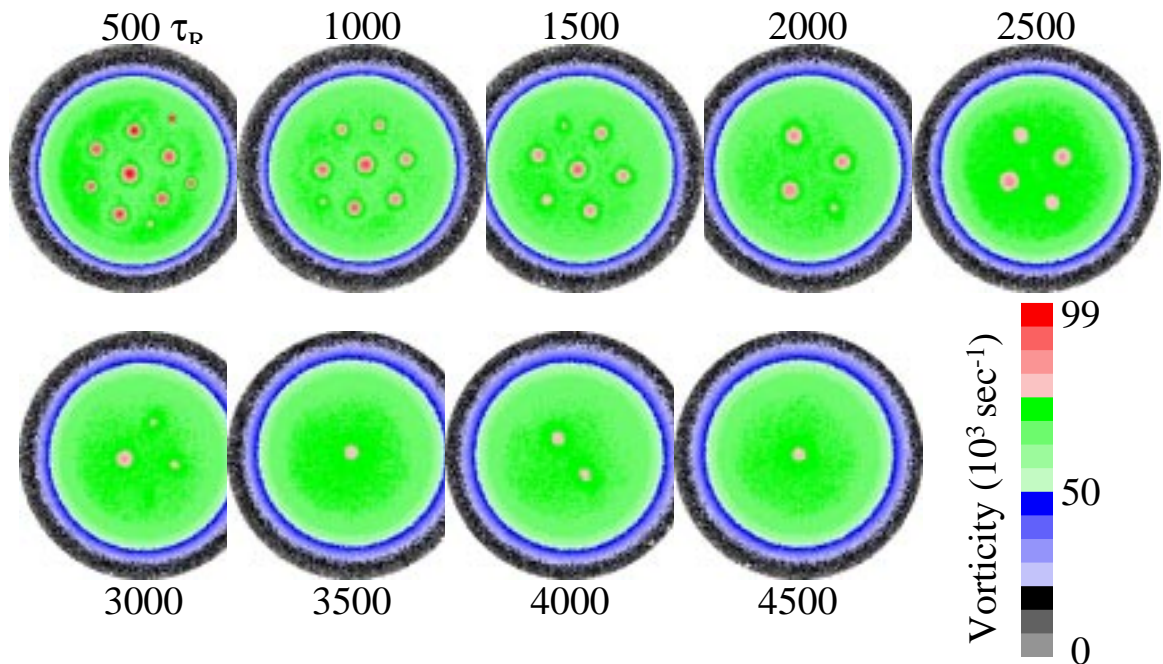
Figure 5. The "melting" of vortex crystals due to dissipative or diffusive effects analogous to viscosity.

Note that as N_v decreases, the remaining vortices re-adjust to a new rigidly rotating, symmetrically spaced pattern.

The images at late times give only a "statistical" picture of the evolution. For example, the Figure 5 images at 3500, 4000, and 4500 τ_R do not indicate that a vortex fissured, but merely reflect the slight shot-to-shot variation observed in N_v for the crystal evolution.

A better example of this shot-to-shot variation is demonstrated in Figure 6, showing 4 shots at time $500\,\tau_R$, repeated with the same initial condition. The images have a "generic" pattern of 6 vortices around a central vortex, with small vortex "defects" varying in number and position.
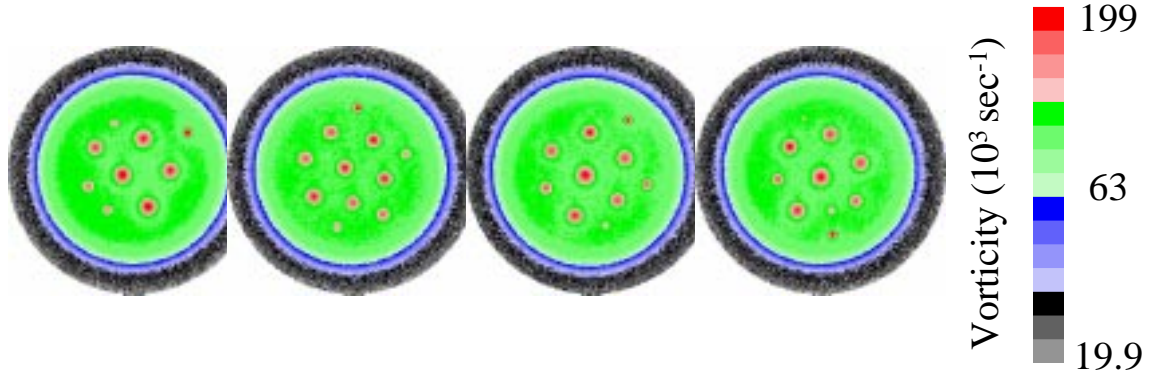
Figure 6. Repeated images at $500\, \tau_R$ taken with identical initial conditions, showing detailed differences in generically similar vortex crystals.

The measured integral quantities, shown in Figure 7, are consistent with 2D inviscid motion on large scales and dissipation on fine scales. From the measured $n(r,\theta)$ we directly calculate the number of electrons per unit length N_L (i.e. fluid circulation Γ_{tot}); the canonical angular momentum (fluid angular impulse) P_θ; the electrostatic energy (fluid kinetic energy) H_ϕ; and the enstrophy Z_2. These are calculated, from $n(r,\theta)$ and $\phi(r,\theta)$ as

$$
\begin{aligned}
N_L &\equiv \int d^2r\, n \\
\Gamma_{tot} &= (4\pi ec\,/\,B)\, N_L \\
P_\theta &\equiv R_W^{-4} \int d^2\mathbf{r}\, r^2\, n\,/\,n_0 \\
H_\phi &\equiv -\frac{1}{2} R_W^{-2} \int d^2\mathbf{r}\, (\phi\,/\,\phi_0)(n\,/\,n_0) \\
Z_2 &= \frac{1}{2} R_W^{-2} \int d^2\mathbf{r}\, (n\,/\,n_0)^2.
\end{aligned}
\tag{4}
$$

The integrals are scaled by the total circulation Γ_{tot} and by the wall radius R_W so as to more generally characterize the evolution. Here, the characteristic density n_0 and the characteristic potential ϕ_0 is

$$
\begin{aligned}
n_0 &\equiv N_L\,/\,R_W^{\,2} \\
\phi_0 &\equiv eN_L.
\end{aligned}
\tag{5}
$$

Experimentally, the circulation, angular momentum, and energy are robust invariants. The circulation shows systematic variations of 10%, probably due to slow variation of the filament emission and slow ionization of background gas

when $t \geq 0.1\,\mathrm{sec}$. This variation of Γ_{tot} does not significantly affect the scaled P_θ or H_ϕ, since they are scaled by n_0. The 5% rise in P_θ at late times indicates a slightly broader column due to apparatus anomalies.

The maximum vorticity ζ_{max} should also be conserved in ideal flow. The measured ζ_{max}, plotted in Fig. 7, shows a 30% increase for the crystals sequence, but no significant change for the monotonic sequence. The reason for this increase is not understood; it may be due to filamentary structures at $t = 0$ which are not initially imaged because they are smaller than the pixel size.

In contrast, the enstrophy Z_2 is a "fragile" invariant, and initially decays a factor of 2 in both sequences. For the crystals sequence, Z_2 is constant from 10 to $10^4 \tau_R$, at which time the individual vortices decay in place.

Reduction of the chaotic advective motions of the individual vortices is required to form the vortex crystal states; this "cooling" is shown in Figure 8. Here, the average
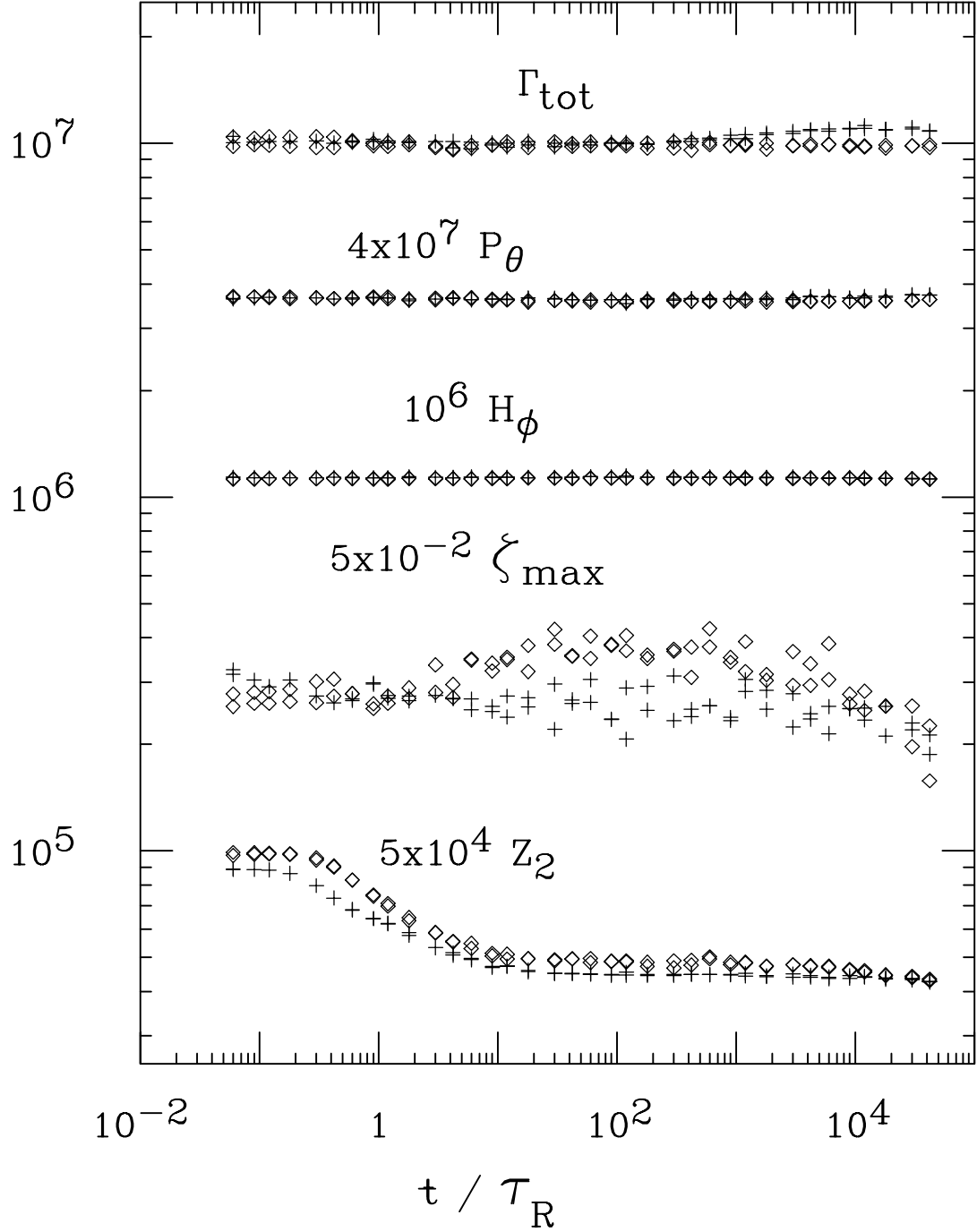
Figure 7. Evolution of the robust invariants of total circulation Γ_{tot}, angular momentum P_θ, and energy H_ϕ; the maximum observed vorticity ζ_{max}; and the fragile enstrophy invariant Z_2 for the two sequences.

magnitude of the random velocities of the individual vortices, $\left|\delta\mathrm{V}\right|$, is relative to the rotating frame in which the mean discrete vortex velocity is zero. The velocities are

23

obtained from the potential $\phi(r, \theta)$ calculated from the measured $n(r, \theta)$ and boundary conditions $\phi(R_W, \theta) = 0$. $|\delta V|$ is normalized to the fluid velocity at the edge of the vortex, V_{edge}, where $V_{edge} = 2\pi R_V / \tau_R = 5.5 \times 10^4 \, cm / sec$.

The measured $|\delta V|$ decreases a factor of 6 between $2 \tau_R$ and $100 \tau_R$ for the crystals sequence, whereas only slight cooling is seen before $N_v = 1$ (and $|\delta V| = 0$ by
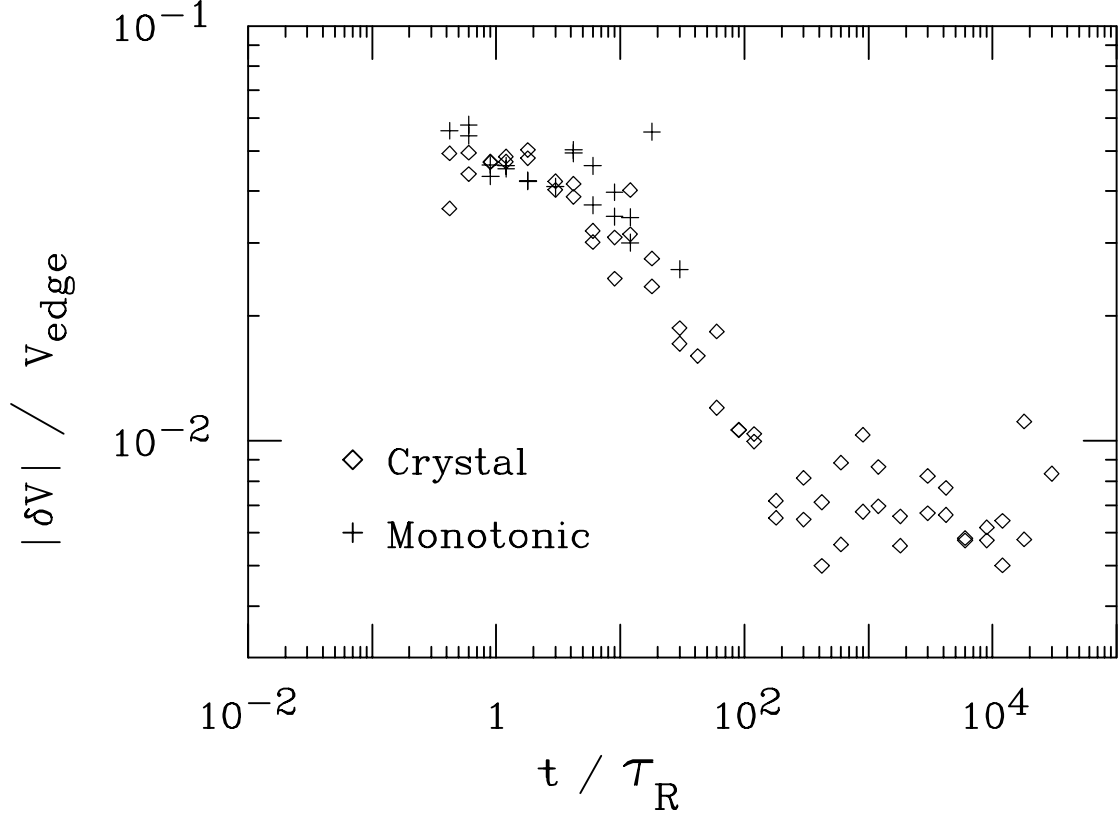
Figure 8. Evolution of the average chaotic vorticity $|\delta V|$ of the vortices for the two sequences, normalized by $V_{edge} = 2\pi R_p / \tau_R = 5.5 \times 10^4 \, cm / sec$.

definition) for the monotonic sequence. The residual $|\delta V|$ for $t \geq 100 \tau_R$ may indicate incomplete cooling, measurement noise, or systematic errors such as uncertainty in the position of the trap axis.

Figure 9 shows a selection of the symmetric crystal patterns which have been observed. Apparently, there are many different "meta-equilibria" to which the system can evolve under near-inviscid 2D dynamics. Experimentally, these meta-equilibria appear to last "forever" ($\tau_R \approx 1 \, sec$), i.e., until plasma diffusive or viscous effects not included in Eqns. (2) act to dissipate the individual vortices. The equilibria observed when the vortices all have essentially the same circulation are closely related to the minimum energy equilibria of point-vortices in a circular domain calculated by

Campbell and Ziff [34]. When the vortex circulations differ substantially, the patterns are less symmetric.
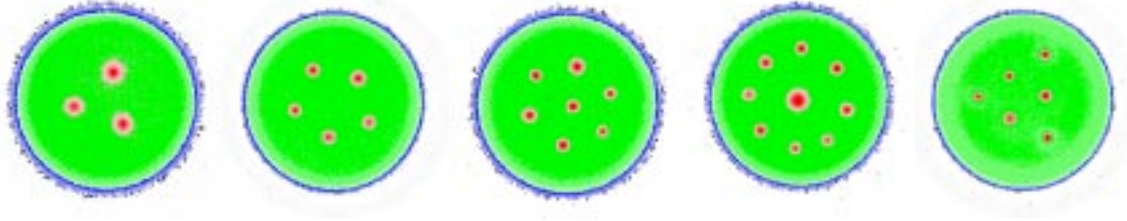
Figure 9. Selection of vortex crystal patterns obtained from initial conditions generally similar to those of Fig. 3.

F. Discussion

Since the discovery of vortex crystals, much theory has been developed by other researchers to describe the dynamics of vortex crystal formation and to predict the final crystal state. A linear theory describes the inward radial motion of a single vortex in a sheared background. Simulations of 2D Euler flow have produced vortex crystals, indicating that cooling is a 2D effect. Theories of vortex cooling describe surface waves of vorticity as carrying away the chaotic energy of the individual vortices. Statistical methods have succeeded in predicting the final crystal pattern and background vorticity profile. However, as yet, the vortex crystal state cannot be predicted from statistics alone.

A linear perturbation theory has been developed to estimate the rate at which an intense vortex moves up a background "hill" of vorticity $d\zeta_0 / d\, r$ [38]. Essentially, the intense vortex located at radius r_v mixes the background fluid, flattening the local vorticity gradient and increasing the background's angular momentum P_θ^{bkg}. To conserve the total angular momentum of the system, the intense vortex moves radially inward. The rate of radial transport $\alpha \equiv d\, r_v / d\, t$ depends on how much fluid within a radius ρ the intense vortex can "trap" around itself in the local shear $d\, \Omega_0 / d\, r$. For intense vortices of circulation Γ_v and radial extent R_v, linear theory predicts $\alpha \propto (d\zeta_0 / d\, r)(d\, \Omega_0 / d\, r)^{-1} \Gamma_v R_v^{-1} \ln(\rho)$. Simulations confirm this rate. Interestingly, simulations show that intense "clumps" of vorticity move up hills of vorticity at a much faster rate than deep "holes" move downhill.

Recent vortex-in-cell computer simulations support our belief that this cooling and cessation of relaxation through mergers is a general 2D fluid effect, i.e., independent of the details of the weak fine-scale viscosity or dissipation. When initialized with simple annular vorticity distributions from recent experiments, the simulations show cooling and relaxation to crystal states at the same rate as experiments, with patterns of

nearly the same vorticity distributions. The relaxation rate depends strongly on the ratio of the circulation in the background to that in the strong vortices [39]. We emphasize that two essential characteristics of this system are the non-zero total circulation and the boundary of the background vorticity patch, which may not be true for other numerical works. For example, hyper-spectral codes which follow evolutions in Fourier space typically use rectangular repeating domains and zero total circulation [26].

It appears that the vortex cooling occurs due to an interaction between the individual vortices and the boundary of the background vorticity. A weak interaction would be described as the excitation of surface waves on the background, and these waves could be damped by the "spatial Landau damping" [12, 35, 36], discussed in Chapter IV. For strong interactions and short wavelengths, this would correspond to entrainment and mixing of low vorticity regions from the edge of the column. Some of the experimental images suggest this latter process, and it has been clearly observed in 2D vortex-in-cell simulations. A similar process may cause negative (relative) vorticity "holes" to become symmetrically situated, as observed in previous experiments [40].

A recent theory describing the vortex crystal states as "regional" maximum fluid entropy states has been surprisingly successful in predicting the observed crystal patterns and the vorticity distribution of the background [41]. The theory is based on the premise that the background is well mixed by the intense vortices, but the fluid within the vortices is not well mixed. It takes as *input* the number and circulation of the surviving vortices; the crystal state is described by maximizing the "regional" fluid entropy of the system, rather than the global fluid entropy. Given the robust conserved quantities Γ_{tot}, P_θ, and H_ϕ, plus the number M and strength Γ_v of the strong vortices which survive the early evolution, the theory predicts the position of the vortices in the crystal and the background vorticity profile $\zeta_0(r)$. Agreement with experiment is impressive. Two factors are used to characterize the crystal state: a geometric factor describing the vortex pattern, and a factor describing the vorticity profile of the background. During typical vortex crystal evolutions, the deviation of the predicted crystal pattern from the measured pattern decreases by a factor of 10, concurrent with a factor of 3 decrease in the deviation of the predicted background profile from the measured profile. Thus during the formation of the vortex crystal, the system approaches a "regional" maximum entropy state.

Although the background is well mixed, fluid trapped within the strong vortices is not. One must assume the number of vortices in the final state; as yet, the final state cannot be predicted from statistics alone. Nor can this system be adequately approximated as point vortices punctuated by occasional merger events: the cooling represents vortex motion which is non-Hamiltonian due to interaction with the

background vorticity. In contrast, experiments on vortex dynamics without a background of vorticity have shown frequencies and instability rates closely corresponding with point vortex theory [42]. It remains to be seen how ubiquitous these crystal meta-equilibria are, and the extent to which non-Hamiltonian dynamical vortex cooling is significant in vortex dynamics even when crystal patterns do not occur.

CHAPTER IV

THE EVOLUTION OF VORTICITY WAVES AND PERTURBATIONS

G. Introduction

We present observations of the evolution of vorticity perturbations, or waves, on
nominally axisymmetric vortices with monotonically decreasing vorticity profiles
$\zeta_0(r)$. Such vorticity perturbations occur spontaneously in turbulent flows when
nearby vortices deform otherwise axisymmetric vortices. In our experiments, we create
sinusoidal perturbations of the form $e^{im\theta}$, with m=2. The evolution can then be
described as coherent waves with extended spatial eigenfunction vorticity $\xi_d(r)$
propagating in θ at a single frequency ω_d.

These waves are generalized versions of the surface waves analyzed by Kelvin [43]
for "top-hat" vorticity patches. The extension of Kelvin waves to large amplitudes (a
"V state") was simulated by Deem and Zabusky using contour dynamics, and is well-
understood analytically [44]. For m=2, the V-state is just an elliptical vortex, rotating
at frequency ω. Known as "diocotron" waves in plasma physics, generalized Kelvin
waves have long been observed on monotonically decreasing vortices in experiments
with magnetized electron columns [45].

Traditional fluid theory has described small vorticity perturbations as a
superposition of "continuum modes" each of which essentially advects with the local
sheared flow. Integral quantities of the perturbed flow, such as the streamfunction
perturbation $\delta\psi$, are predicted to decrease in time as $\delta\psi \propto t^{-\alpha}$, where $\alpha \approx 1-2$

[46]; the vorticity perturbation is "sheared apart" as continuum waves "phase mix." However, we will see that the generalized Kelvin wave may persist for long times, either because it is a "discrete" wave which is actually undamped, or because it is a "quasimode" with damping suppressed by nonlinear effects.

The linear theory of Briggs, Daugherty and Levy [12] decomposes small perturbations into a superposition of eigenmodes consisting of a countable number of discrete waves and an infinite number of continuum modes. A collection of continuum modes which is in phase initially will phase-mix over time, leading to the expected algebraic decay. Under some circumstances, a band of continuum modes appears to be a single "quasimode" which damps exponentially. However, the discrete waves persist indefinitely, and thus may dominate the evolution.

The undamped discrete wave exists if the vorticity profile $\zeta_0(r)$ is zero at the "critical radius" r_c where the fluid rotates at the wave phase velocity. For profiles with non-zero vorticity at $r = r_c$, linear theory [12] predicts that the small amplitude Kelvin waves are "quasimodes" which decay as $e^{-\gamma t}$. This inviscid decay has been analyzed for simple profiles $\zeta_0(r)$ to obtain quasimode frequency ω_q and damping rate γ [47] and has been observed in prior experiments [36].

We observe the exponential decay of quasimode amplitudes $A_q(t)$ over the first 5 wave periods of the evolutions. Decay rates γ are closely predicted by a computer code which uses our measured $\zeta_0(r)$ and solves the linearized Euler equations [13]. The eigenmode method allows numerical calculations of the quasimode structures [48], which agree well with the measured waves.

29

Surprisingly, in our laboratory experiments, we do not observe any continuum mode response. Even at early times, the discrete Kelvin wave is at least 10 times greater in amplitude than the continuum modes, which are at most at the level of experimental noise. Using our measured $\zeta_0(r)$, we numerically solve for the discrete and continuum modes, and find that outside perturbations excite the discrete mode much more strongly than the continuum modes. In essence, by its nature, the Kelvin wave couples well with applied multipole fields.

Large vorticity perturbations complicate this linear damping picture. The perturbations launched and detected in our experiments are always nonlinear in that they never fully decay away. After $5-10$ wave periods of exponential decay, the quasimode amplitude "bounces" back up, and then oscillates about some intermediate value. In essence, the wave decay halts because there is insufficient vorticity at the critical layer to damp the total wave energy. Images of $\zeta(r,\theta)$ show vorticity filaments forming Kelvin's "cat's eye" structures. Within these "cat's eyes," trapped fluid moves in and out of phase with the wave, modulating the wave amplitude at a "trapping frequency" which scales as $f_{to} \propto A_q^{1/2}$. The final cat's eye structure is stable, and lasts for up to $10^4 \, \tau_R$, until viscosity "smears" out the filaments. Thus, despite the inviscid decay process, we find that for damped or undamped Kelvin waves, vortices may resist symmetrization.

A final limitation on applying linear theory demonstrated by our experiments is that large vorticity perturbations may modify the profile $\zeta_0(r)$, even though this is precluded in linear theory. Typically, large amplitude perturbations transfer vorticity

radially outward past the critical layer. Even if ζ_0 has $\zeta_0(r_c) = 0$ at small amplitudes, for large amplitudes, the perturbed vortex can exhibit inviscid damping and forms "cat's eyes."

H. Description of Experiments

The experiments start with a centered, azimuthally symmetric column of electrons, i.e., a centered, symmetric vortex well separated from the wall. Typical electron densities are $n \approx 2 \times 10^6 \text{ cm}^{-3}$, with typical column radii $R_V \approx 1 \text{ cm}$. The vorticity is $\zeta \approx 10^5 \text{ sec}^{-1}$, and the vortex rotation (turnover) time is

$\tau_R = 4\pi / \zeta \approx 150\,\mu\text{sec}$. The electron density versus radius in this column can be controlled experimentally, and several different vorticity profiles $\zeta(r)$ will be presented.

We make this vortex non-symmetric by applying θ-dependent voltages to part of the containment wall. Two of the containing cylinders, labeled S_4 and S_8 on Fig. 1, have cutout wall patches with 4- and 8-part θ-symmetry, electrically isolated from the cylinder frame. To excite an m=2 perturbation, we apply voltages to cylinder S_4 in an m=2 symmetric fashion (as indicated in Fig. 2) for one-half wave period of the m=2 discrete mode. The perturbation is imposed by applying (-5, +5, -5, +5) volts to the 4 azimuthal sectors of containment cylinder S_4 for a duration of 55 μsec. In the fluid picture, this applied voltage changes the $\mathbf{E} \times \mathbf{B}$ velocity field from a symmetric flow to an m-multipole flow which falls off like r^{m-1} inside the cylinder. Thus a m=2 wall voltage is analogous to an applied dipole flow field.

31

This dipole flow field causes the initially symmetric vortex to become elliptical, with an ellipticity controlled by the strength and duration of the applied voltage. The applied voltage is then removed, and we study the free evolution of the asymmetric vortex, i.e., the evolution of "waves" on the otherwise symmetric vortex. The evolution is diagnosed through measurements of $\zeta(r,\theta,t_i)$ at times t_i using the phosphor/CCD camera imaging system.

In addition to destructively measuring $\zeta(r,\theta,t_i)$ with the CCD camera, we also non-destructively measure the far-field quadrupole moment of the perturbed wave vorticity throughout the evolution. The perturbation induces image charges on the wall sectors of the 8-part probe S_8. For a m=2 perturbation, as indicated in Figure 2, we combine signals from opposite sectors to detect wave amplitudes and frequencies.

I. Generalized Kelvin Waves

For "top-hat" vortices with vorticity profile

$$\zeta_0(r) = \zeta_0, \quad r < R_V, \\ 0, \quad r \geq R_V$$
(6)

where R_V is the vortex radius, Kelvin linearized the Euler equations in an infinite domain. In polar coordinates, with

$$\zeta(r,\theta,t) = \zeta_0(r) + \delta\zeta(r,\theta,t) \\ \psi(r,\theta,t) = \psi_0(r) + \delta\psi(r,\theta,t),$$
(7)

the linearized equations are

$$\frac{\partial \delta \zeta}{\partial t} + \Omega_0(r) \frac{\partial \delta \zeta}{\partial \theta} - \frac{1}{r} \frac{d\zeta_0}{dr} \frac{\partial \delta \psi}{\partial \theta} = 0$$

$$[\frac{\partial^2}{\partial r^2} + \frac{1}{r} \frac{\partial}{\partial r} + \frac{1}{r^2} \frac{\partial^2}{\partial \theta^2}] \delta \psi = \delta \zeta, \tag{8}$$

where $\Omega_0(r) = \psi_0(r)/r$. Solving for perturbations of the form

$$\delta \zeta(r,\theta,t) = \xi^{(m)}(r) e^{im\theta - i\omega^{(m)}t}$$

$$\delta \psi(r,\theta,t) = \psi^{(m)}(r) e^{im\theta - i\omega^{(m)}t}, \tag{9}$$

the linearized equations are

$$[\omega - m\Omega_0(r)] \xi^{(m)} + \frac{m}{r} \frac{d\zeta_0}{dr} \psi^{(m)} = 0$$

$$\left\{ \frac{\partial^2}{\partial r^2} + \frac{1}{r} \frac{\partial}{\partial r} - \frac{m^2}{r^2} \right\} \psi^{(m)} = \xi^{(m)}. \tag{10}$$

Kelvin found surface waves at the vortex edge [43] with wave structure

$$\xi^{(m)}(r) \propto \delta(R_V), \tag{11}$$

propagating in θ with frequency

$$\omega^{(m)} = \frac{\zeta_0}{2}(m-1). \tag{12}$$

Later work included a free-slip wall at $r = R_W$ [49]: the Kelvin wave remains a delta-function perturbation on the surface of the vortex patch, but the frequency is shifted slightly, as

$$\omega^{(m)} = \frac{\zeta_0}{2}[(m-1) + (\frac{R_V}{R_W})^{2m}]. \tag{13}$$

A slightly smoothed top-hat vortex with $R_V = 0.3$ and $R_W = 1.0$ is plotted in Fig. 10 (top).

Here, we investigate Kelvin waves on more general $\zeta_0(r)$. The vortices considered are monotonically decreasing monopoles. Two examples are shown in Figure 10, namely where $\zeta_0(r) = e^{-(\frac{r}{R_V})^4}[1-(r/R_W)^4]$ (Fig. 10 middle) and

$\zeta_0(r) = e^{-(\frac{r}{R_V})^2}[1-(r/R_W)^4]$ (Fig. 10 bottom). $R_V = 0.3$ and $R_W = 1.0$ for both profiles. These vortices create flow fields $v_\theta(r)$, or equivalently, angular rotation profiles $\Omega_0(r)$, given by

$$\Omega_0(r) \equiv \frac{v_\theta(r)}{r} = \frac{1}{r^2}\int_0^r r\, dr\, \zeta_0(r).\tag{14}$$

As early as 1880, Kelvin noted "a disturbing infinity" [50] in the linearized Euler equations for $e^{im\theta}$ perturbations on vortices with nonzero ζ_0 and $d\zeta_0/dr$ at critical radii r_c. The critical radius is where the fluid rotates at the phase velocity of the Kelvin wave, defined by

$$\omega^{(m)} - m\Omega_0(r_c) = 0.\tag{15}$$

For profiles with $d\zeta_0/dr\big|_{r_c} \neq 0$, modern linear theory [12] predicts that small amplitude Kelvin waves decay as $e^{-\gamma t}$. In this inviscid process, resonant fluid is transported across r_c so as to flatten the local vorticity gradient $d\zeta_0/dr\big|_{r_c}$. Thus the wave decay rate $\gamma \propto d\zeta_0/dr\big|_{r_c}$.
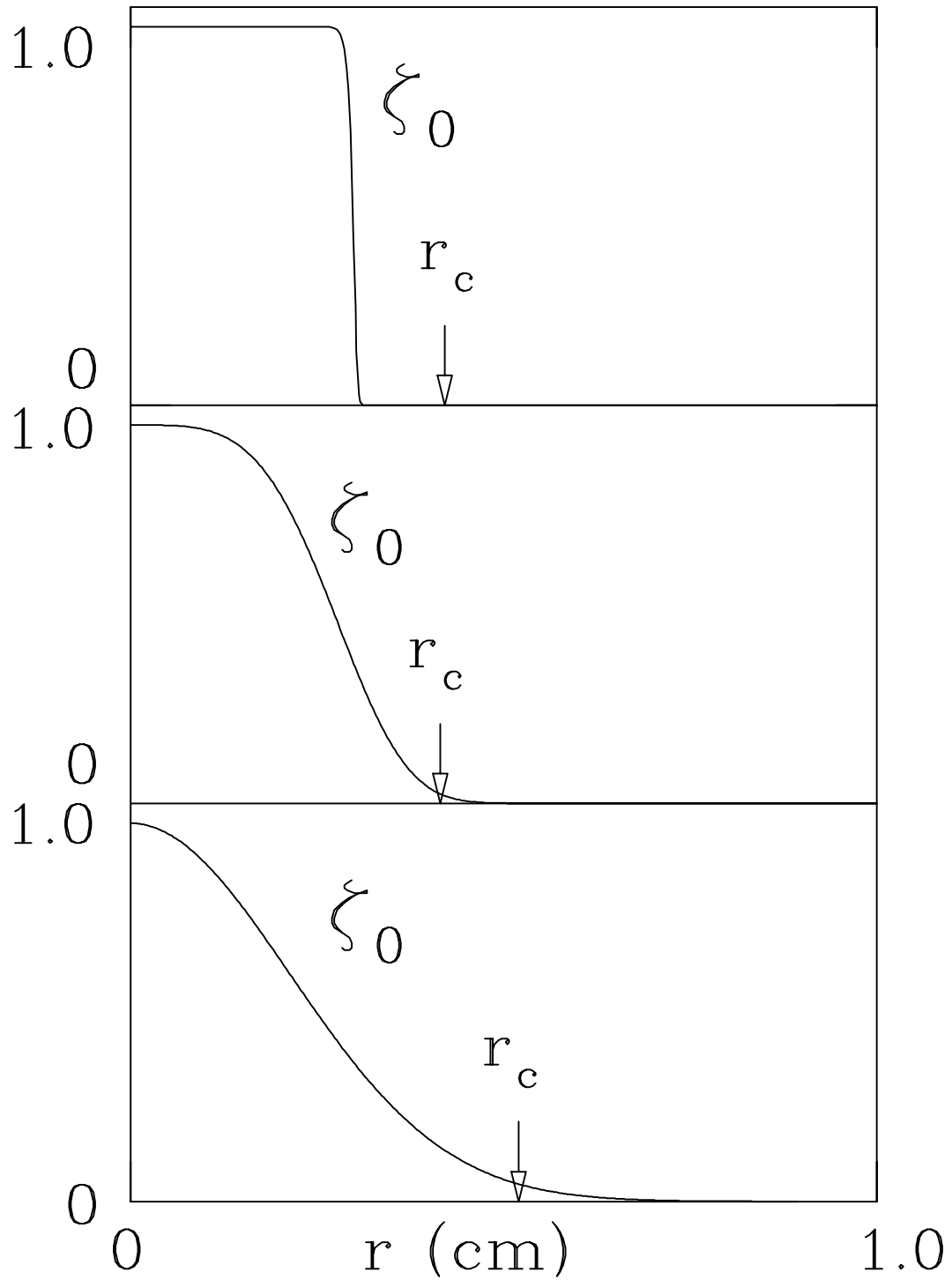
Figure 10. Model vorticity profiles ζ_0: smoothed top-hat, exponential with power 4, and exponential with power 2 (gaussian). The arrow indicates the critical radius r_c for m=2 Kelvin waves on each vortex.

For top hat profiles, r_c is easily calculated and is always outside the vortex; that is, $R_W > r_c > R_V$. In this simple case, $\gamma = 0$. In Figure 10 (top), the arrow indicates the critical radius $r_c = 0.42$ for the m=2 Kelvin wave.

For more general $\zeta_0(r)$, such as those plotted in the middle and bottom of Figure 10, r_c may fall within the vortex, $r_c < R_V$. We use a numerical method described in Section E to solve for the m=2 Kelvin wave on generalized profiles. For the middle and bottom profiles we find $r_c = 0.415$ and $r_c = 0.52$, respectively. For the middle profile, the decay rate γ / ω_q of so-called quasimodes is $\gamma / \omega_q = 0.01$; the Kelvin quasimode would thus exhibit exponential decay, decreasing in amplitude by one factor of e every $N_\gamma \equiv \omega_q / 2\pi\gamma = 16$ cycles. For the gaussian profile from Figure 10 (bottom), we find $\gamma / \omega_q = 0.4$, so quasimodes decay in less than one wave period; here, it is questionable whether there is much utility in speaking of a quasimode. This agrees with the rapid generation and phase mixing of vorticity filaments noted in simulations using a gaussian profile by Bernoff and Lingevitch [51]. In this work, no wave-like behavior was apparent, and the focus was on the time scale in which these fine scale filaments were dissipated by a viscous "shear-diffusion" mechanism.

J. Experimental Results

One set of wave experiments utilized a θ-symmetric vortex with the strongly peaked vorticity profile $\zeta_0(r)$ and $\Omega_0(r)$, shown in Figure 11 (top).

Figure 11. The measured vorticity ζ_0 and angular rotation Ω_0 for a vortex with weak wave damping. Also shown is the initial m=2 vorticity perturbation $\delta\zeta(r, t = 0)$ (dashed) and the measured discrete eigenfunction $\xi_d^{\,\mathrm{exp}}$ (solid).
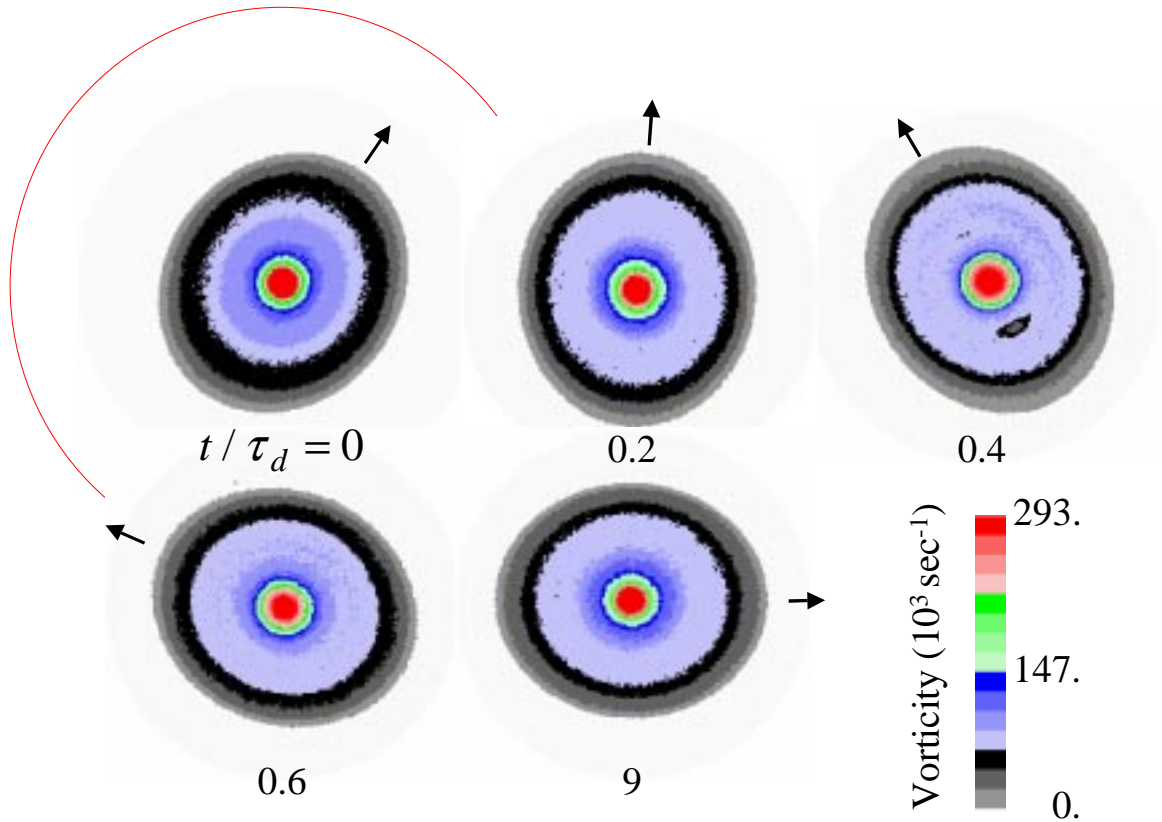
Figure 12. Images of the total vorticity $\zeta(r,\theta,t)$ at five times after a m=2 perturbation was applied to the vortex of Figure 11.

An elliptic perturbation imposed on this vortex is observed to propagate around the vortex as an undamped wave. This "discrete diocotron" wave is the generalization of Kelvin waves on top-hat vortex patches to waves on smooth vortex profiles $\zeta_0(r)$. Figure 12 shows the measured fluid vorticity at 5 times after the wall voltage is turned off. The first image shows the initial elliptical distortion of the vortex in response to the perturbation. Images at later times demonstrate that this elliptical wave of vorticity propagates essentially intact, at frequency $f_d \equiv \omega_d / 2\pi = 9.25$ kHz. The times in Fig. 12 are scaled to the wave period $\tau_d \equiv 1/f_d$.

We analyze the measured perturbation in terms of Fourier components, as

$$\zeta(r,\theta,t) = \zeta_0(r,t) + \sum_{m=1,2,\dots} \delta\zeta^{(m)}(r,t)\, e^{im\theta}. \tag{16}$$

In this paper we will consider only applied $m = 2$ perturbations and $m=2$ responses of the vortex, so we do not write the superscript (2). The $m=2$ response $\delta\zeta(r,t)$ is obtained from the measured $\zeta(r,\theta,t)$ as

$$\delta\zeta(r,t) = \delta\zeta^{(2)}(r,t) = \int_0^{2\pi} d\theta\, \zeta(r,\theta,t)\, e^{-2i\theta}. \tag{17}$$

The initial $m=2$ perturbation from the first image of Fig. 12, $\delta\zeta(r,t=0)$, is plotted as the dashed line in Fig. 11 (bottom).

The measured images determine the radial profile $\xi_d^{\exp}(r)$ of the propagating "diocotron" or "Kelvin" wave, as well as the wave frequency ω_d. We obtain $\xi_d^{\exp}(r)$ by fitting $\delta\zeta(r,t)$ measured at 5 times during 1/2 wave period to the propagating wave functional form

$$\delta\zeta(r,t) = \xi_d^{\exp}(r)\, e^{i\omega_d t}\, e^{\gamma t}. \tag{18}$$

We find $\omega_d / 2\pi = 9.25\ \mathrm{kHz}$, the same as measured in wall signals. The wave profile $\xi_d^{\exp}(r)$ thus obtained is plotted as a solid line in Fig. 11 (bottom); the error bar shows the typical uncertainty of the fit. The wave profile $\xi_d^{\exp}(r)$ is essentially the same as
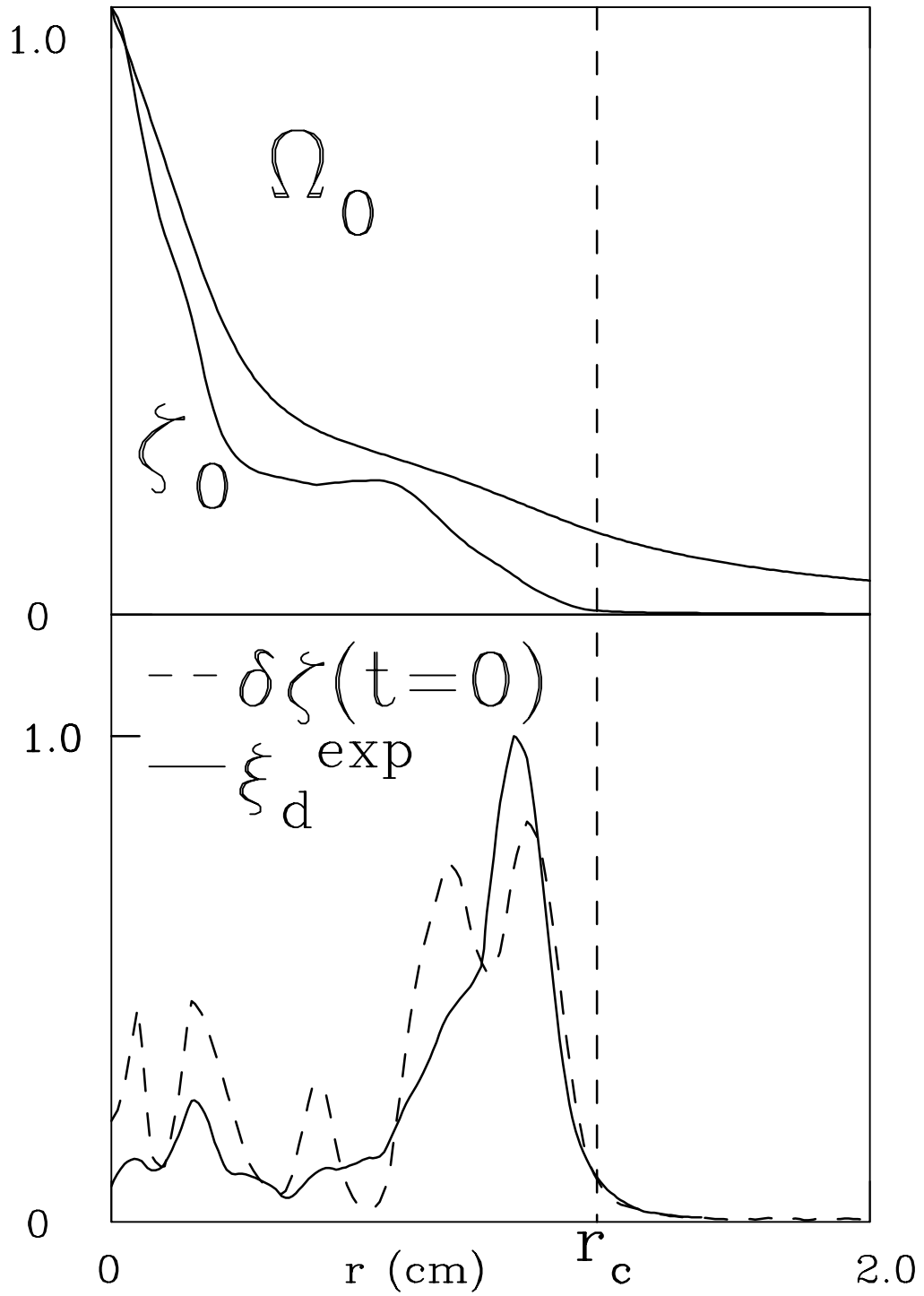
Figure 13. The measured vorticity ζ_0 and angular rotation Ω_0 for a vortex with strong wave damping. Also shown is the initial m=2 vorticity perturbation $\delta\zeta\,(t=0)$ (dashed); and the measured quasimode $\xi_q^{\,\text{exp}}$ (solid).
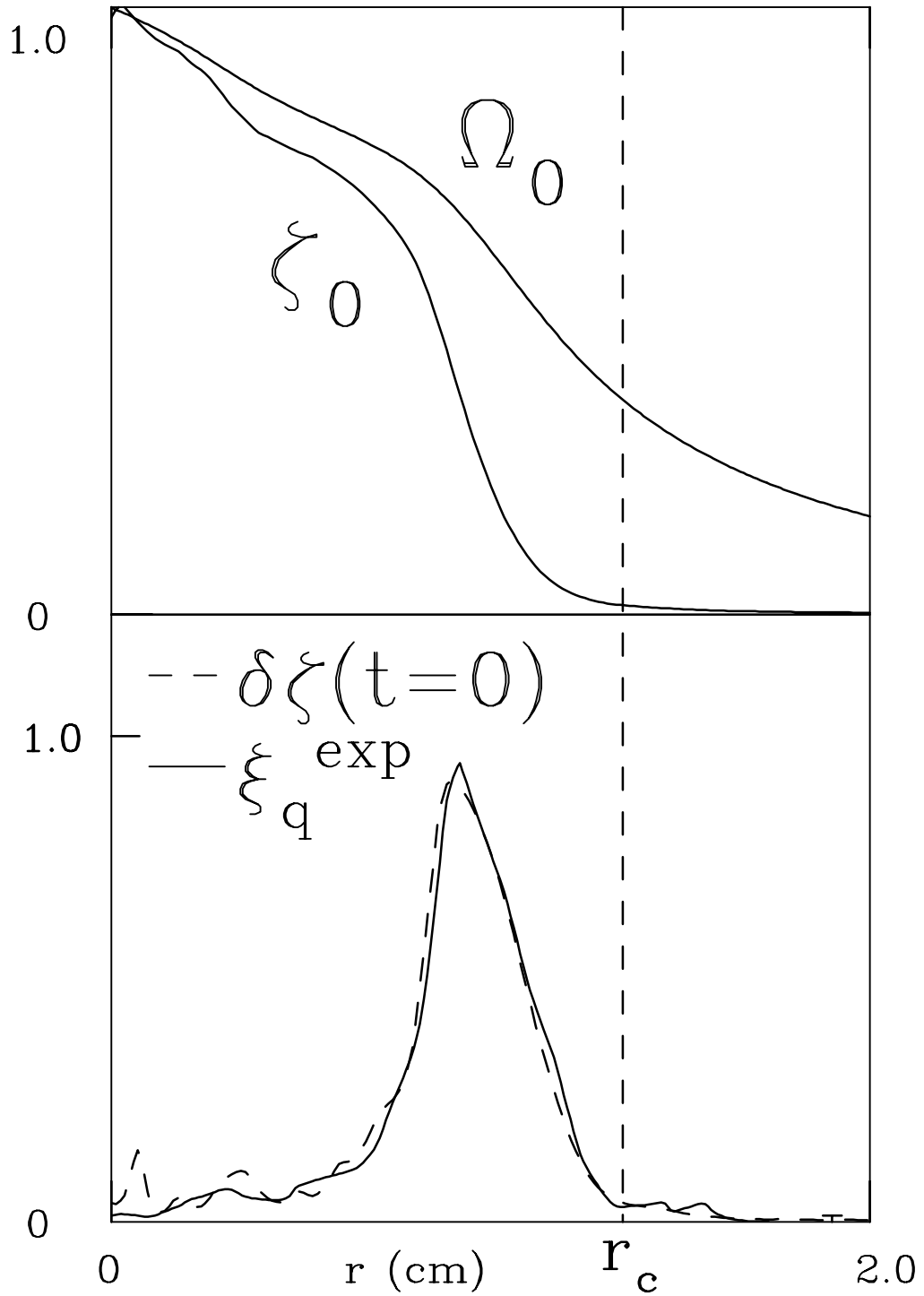
the initial perturbation $\delta\zeta(r, t = 0)$, indicating that only one wave was excited. The

unique character of this "discrete" mode compared to the multitude of "continuum"

modes will be treated in Section E.

The fit to the data gives $\gamma \approx 0$, as the wave is observed to stay at the same

amplitude for the 10 wave periods of detailed observation. Other observations show

that these waves persist for hundreds to tens of thousands of wave periods.

This wave does not decay because there is essentially zero vorticity at the critical

radius r_c, where the wave is resonant with the background flow; r_c is determined from

$$\omega_d = m\Omega_0(r_c), \qquad (19)$$

and is plotted as a dashed line at $r_c = 1.28\text{ cm}$ in Figure 11.

In contrast, when the initial vortex has substantial vorticity at the critical radius,

the wave is observed to decay with time. In this case, theorists prefer to call the wave a

"quasimode." Linear theory suggests that the wave will decay as $e^{-\gamma t}$, but nonlinear

effects generally cause the wave amplitude to oscillate, after which the damping

ceases, with the wave persisting at some finite level.

This inviscid damping is exhibited by the vorticity profile $\zeta_0(r)$ and resulting

rotation profile $\Omega_0(r)$ shown in Figure 13 (top). Here, a 9 volt m=2 perturbation

applied to the wall sectors for 33 μsec creates the elliptical distortion, the evolution of

which is shown in Figure 14. The dashed circle indicates the position of the critical
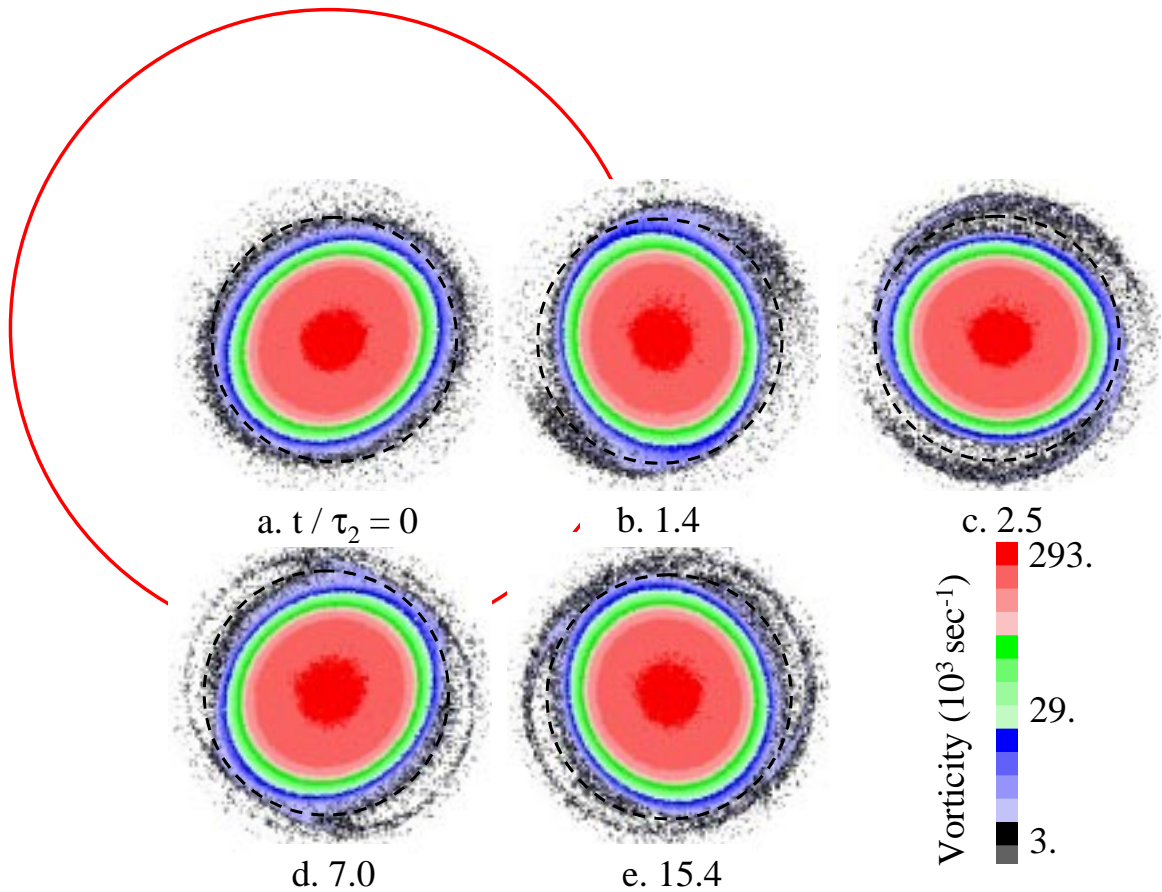
layer r_c.

Figure 14. Images of the total vorticity $\zeta(r,\theta,t)$ at five times after a m=2 perturbation was applied to the vortex ζ_0 of Figure 13. The dashed circle indicates the location of the critical layer r_c.

Now the elliptical vortex generates filaments of vorticity at radius r_c, and these filaments rotate somewhat more slowly than the core. By several wave periods, these filaments wrap up and link, trapping fluid particles in nonlinear Kelvin's "cat's eye" structures. The cat's eye structure then persists in form for thousands of wave periods, slowly dissipating only due to non-ideal effects.

Using the fit described earlier, we determine a quasimode wave profile $\xi_q^{\text{exp}}(r)$, plotted solid in Fig. 13 (bottom), and a wave frequency of $f_q = 15.0\,\text{kHz}$, confirmed by wall signals. The fit to the first 2 wave periods also determines a damping coefficient of $\gamma / \omega_q = 3.5 \times 10^{-2}$.

The quasimode amplitude first damps exponentially, then "bounces" due to "trapping oscillations," then asymptotes at a finite level. To measure this, we determine the quasimode amplitude $A_q(t)$ which best describes the m=2 component of measured image $\delta\zeta(r,t)$, as

$$\delta\zeta(r,t) = A_q(t)\,\xi_q^{\text{exp}}(r), \tag{20}$$

with the wave profile $\xi_q^{\text{exp}}(r)$ already determined by the fit to early-time data. Specifically, at each time t we determine the single number A_q which minimizes the difference between $A_q(t)\xi_q^{\text{exp}}(r)$ and the measured $\delta\zeta(r)$; given the relatively noise-free image data, this number is determined with high precision.

Figure 15 shows that the quasimode amplitude $A_q(t)$ first decreases exponentially to about 55% of the initial amplitude, then *increases* to 90%, then oscillates again; the wave eventually asymptotes at about 75% of the initial amplitude.

This inviscid decay and oscillation can also be seen with an independent measure of the wave amplitude, namely the m=2 (quadrupole) component $Q_2(t)$ of the flow field induced at the wall,
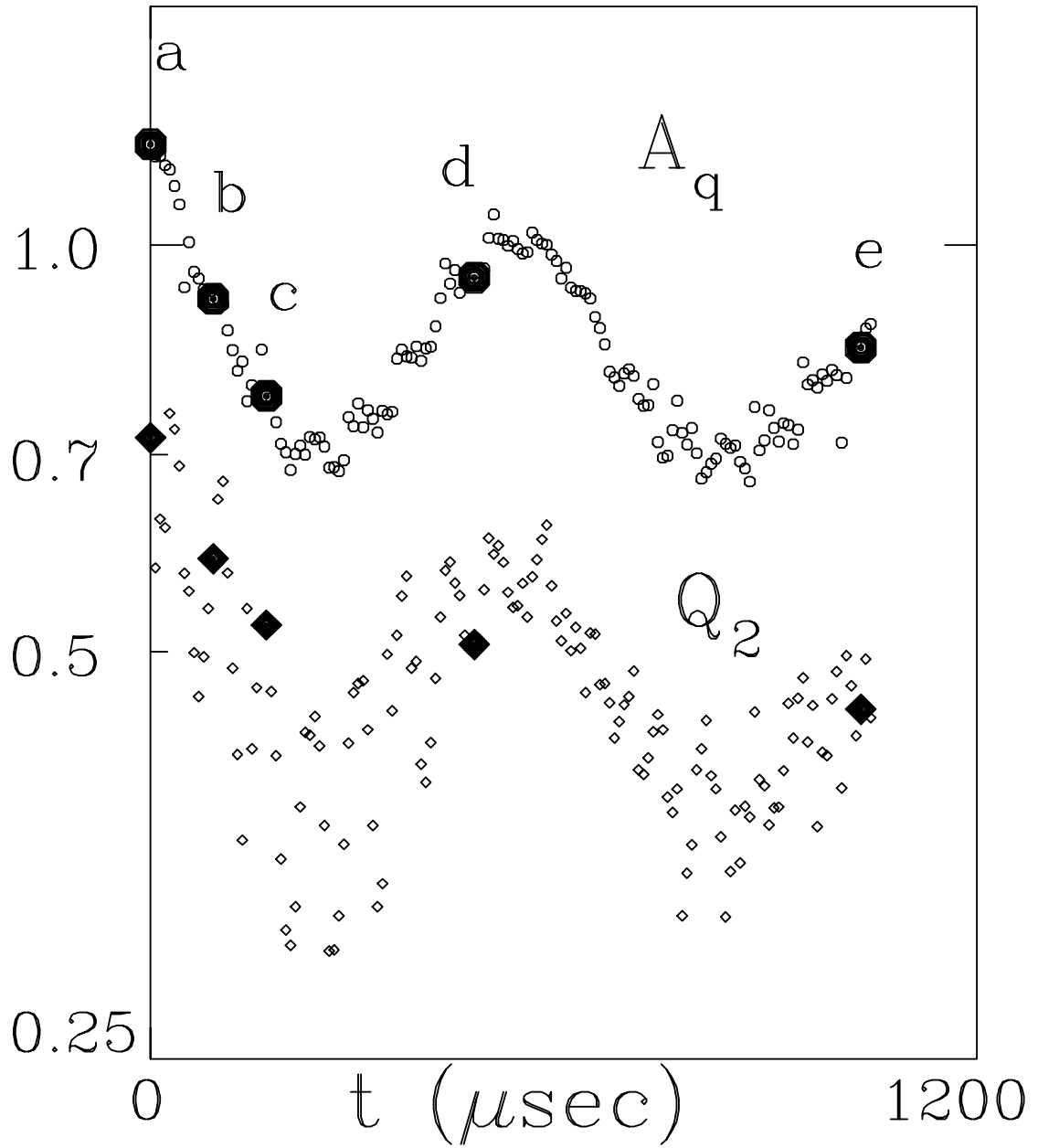
Figure 15. Evolution of the quasimode amplitude A_q and the quadrupole moment Q_2, showing initial exponential decay followed by amplitude bounces.

$$Q_2 \equiv \frac{\int dA' \, (x'^2 - y'^2) \, \zeta(x', y', t)}{\int dA' \, (x'^2 + y'^2) \, \zeta(x', y', t)}, \qquad (21)$$

where x' and y' are the coodinates in a frame with origin at the vortex center and axes

parallel to the ellipse's major and minor axes. The measured $Q_2(t)$ shown in Fig. 15

agrees in all essential aspects with the measured $A_q(t)$, although the calculation of Q_2

has considerably more noise, due to imaging anomalies.

We note that the measured quasimode maintains the same radial profile $\xi_q^{\exp}(r)$

everywhere except at the critical radius, even as the amplitude oscillates with time.

Figure 16 shows the measured vorticity perturbations $\delta\zeta(r, t)$ (solid curve) and

$A_q(t) \, \xi_q^{\exp}(r)$ (dashed curve) at the 5 labeled times in Figs. 14 and 15. The quasimode

shrinks and grows proportionally at all radii, except for the weak filamentary

perturbation at r_c. Thus, wave damping is *not* effected by vorticity at r_c getting out of

phase with the core perturbation and merely canceling the quadrupole moment of the

far field. Rather, the vorticity at r_c perturbs the flow in the vortex so as to cause the

ellipticity of the vortex core to decrease.

In the sequence described by Figs. 14, 15, and 16, when the "cat's eyes" form,

linear damping theory no longer gives an adequate description. Fluid particles

executing trapped orbits move in and out of phase with the core, modulating the

quasimode amplitude $A_q(t)$ at the "trapped" orbit frequency f_{to}. For the data of Fig.

15, we find $f_{to} = (535 \, \mu\sec)^{-1} = 1.9 \text{ kHz}$. We have measured the dependence of this
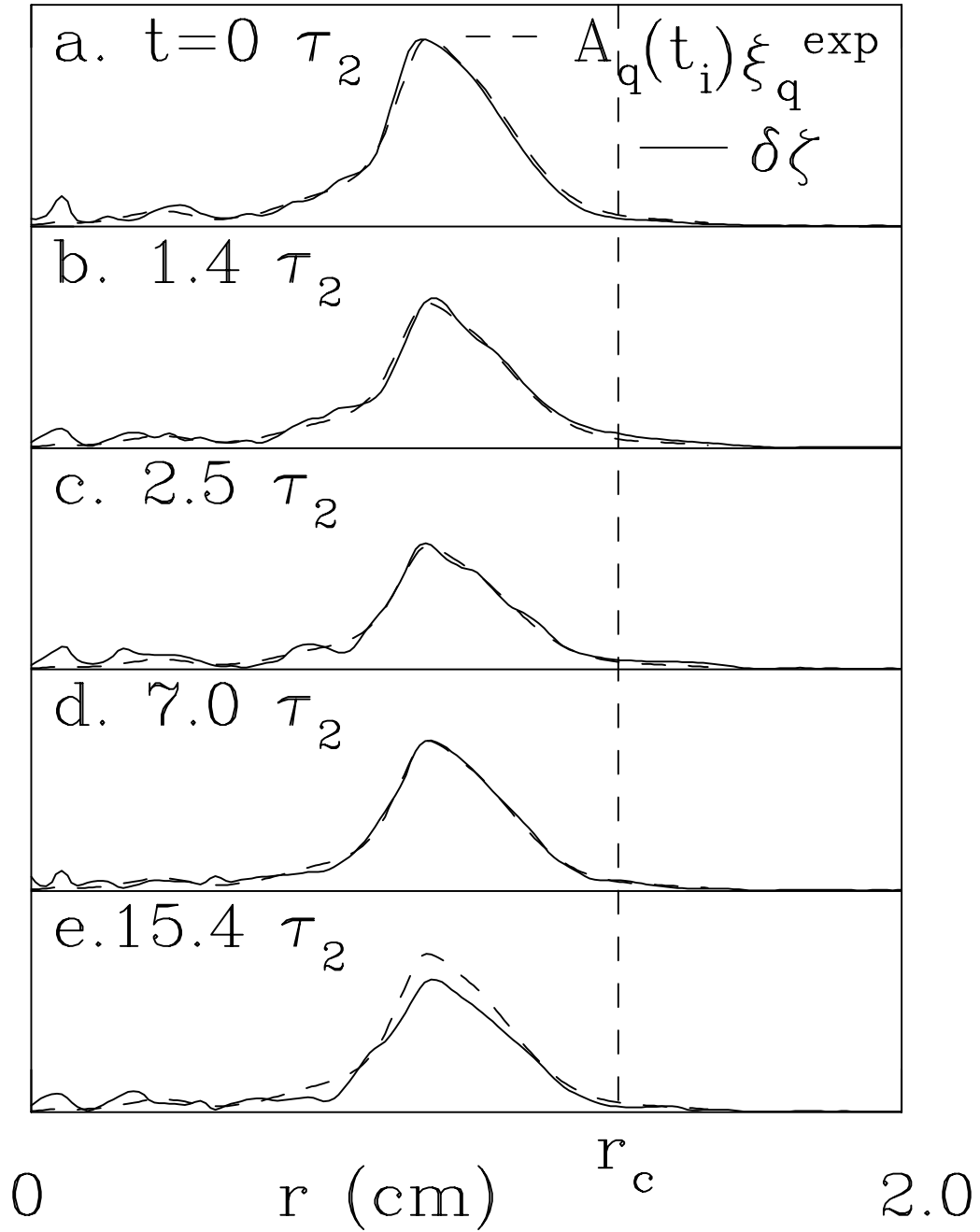
Figure 16. The measured m=2 vorticity perturbation $\delta\zeta(r,t)$ (solid) compared to the quasimode contribution $A_q(t)\,\xi_q^{\mathrm{exp}}(r)$ (dashed curve) at the 5 marked times during the evolution shown in Figure 14.

trapped orbit frequency on quasimode amplitude, represented by the quadrupole moment in Figure 17.

Here, the data represented by squares is obtained from sequences of images such as Fig. 15; and the data represented by x's is obtained from the amplitude of image charges induced on the wall sectors. Since $Q_2 \propto A_q$, we find that the data is roughly described by $f_{to} \propto A_q^{1/2}$, as predicted by theory. This scaling is consistent with trapping theory, with the dynamics shown in Fig. 14, and with the experiments of Pillai and Gould [36].
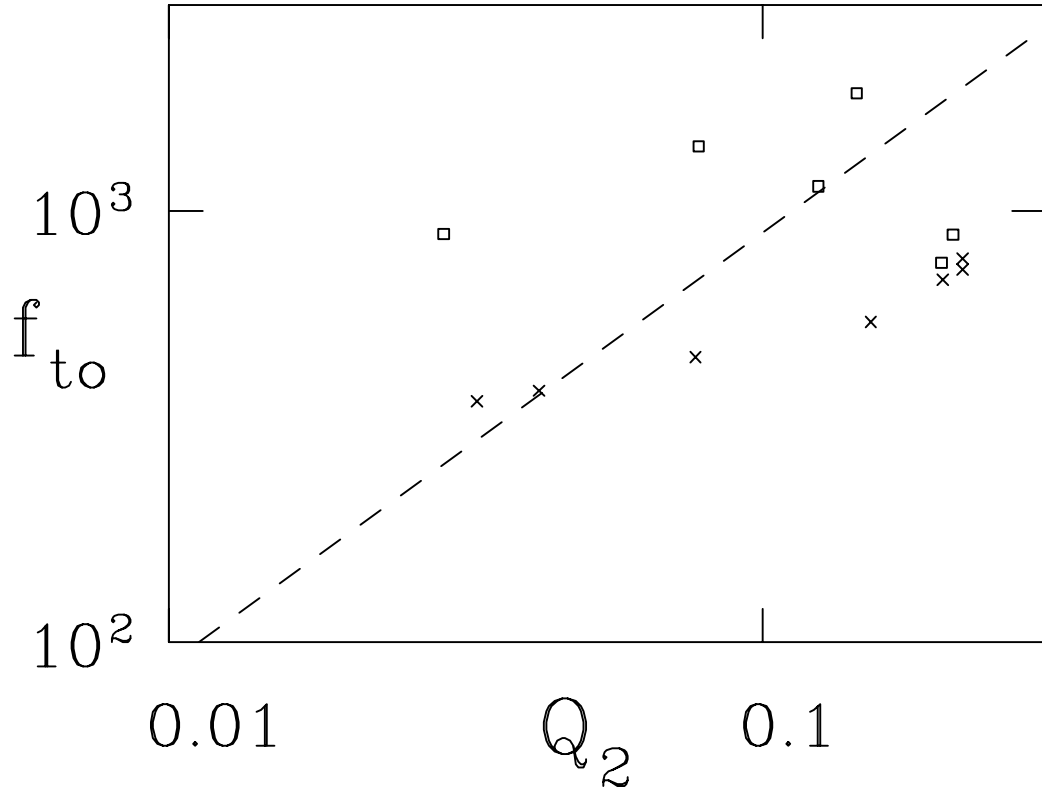
Figure 17 The trapping oscillation frequency f_{to} versus quadrupole moment Q_2 measured from wall signals (x's) and images (squares).

Ultimately the mode amplitude settles to 75% of $A_q(t=0)$. Within a width Δx around the critical layer, vorticity shifts so as to flatten the local θ-averaged gradient $d\zeta_0 / dr \big|_{r_c}$. Once the vorticity gradient is flattened, the damping (or bouncing) stops. Thus, if a quasimode has sufficient amplitude initially, it may persist indefinitely after flattening the vorticity profile at the resonant radius.

One further limitation to the linear wave perspective is that large amplitude perturbations may exhibit inviscid damping and cat's eye formation even when r_c is outside the initial vortex; this is because the large amplitude perturbation modifies

1.0 ζ_0 ζ_e 0.01

0   0

0   r (cm) r_c 2.5

Figure 18. The measured theta-averaged vorticity ζ_e with a large elliptical perturbation (dashed), compared to the profile ζ_0 with no perturbation (solid). The edges of the two profiles are also shown with a y-axis scale of 0 to 0.01.

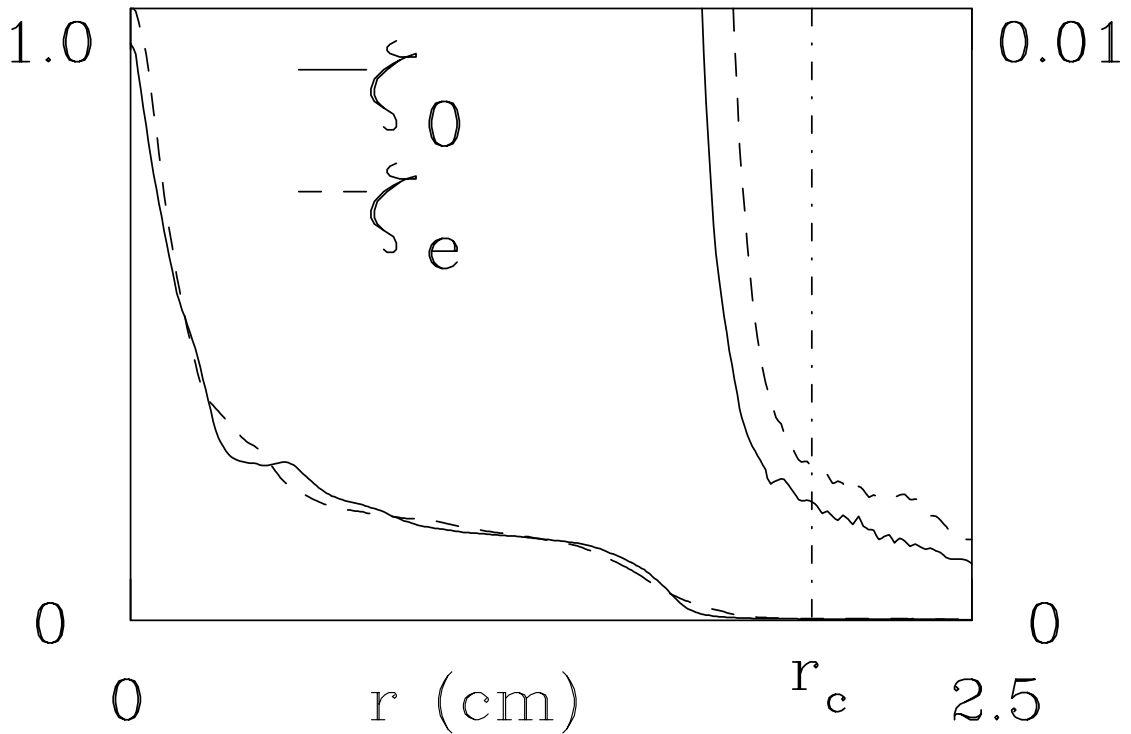$\zeta_0(r)$. Figure 18 shows a profile $\zeta_0(r)$ on which the discrete mode propagates essentially undamped, because $\zeta_0'(r_c) \approx 0$. When we distort the vortex to an ellipse with minor-to-major axis aspect ratio $\lambda \equiv b/a = 0.9$, filaments are observed to form from the ends of the ellipse at r_c. The θ-averaged vorticity profile $\zeta_e(r)$ of the ellipse, shown in Fig. 18, extends further in radius than $\zeta_0(r)$. Of course, this profile modification is outside the domain of linear theory, where all perturbations vary as $e^{im\theta}$ and thus make no change in the θ-averaged profile present.

Finally, Figure 19 graphically illustrates a large-amplitude wave with fully formed cat's eye structures. This state was obtained by continuously driving the m=2 wave for approximately 750 wave periods. As the wave became large, the vorticity distribution extended to r_c, and filaments formed. However, the continuously driven wave remained large, and the net effect of the filaments was to flatten the θ-averaged vorticity distribution around r_c. The flow shown in Fig. 19 is essentially stationary in the rotating wave frame, and is observed to persist for more than 3000 wave periods, after which non-ideal viscous or diffusive effects cause the filaments to broaden and fill in the cat's eyes structure. We note that stationary states essentially identical to Fig. 19 have been obtained in point-vortex simulations of a similar $\zeta_0(r)$ [52].
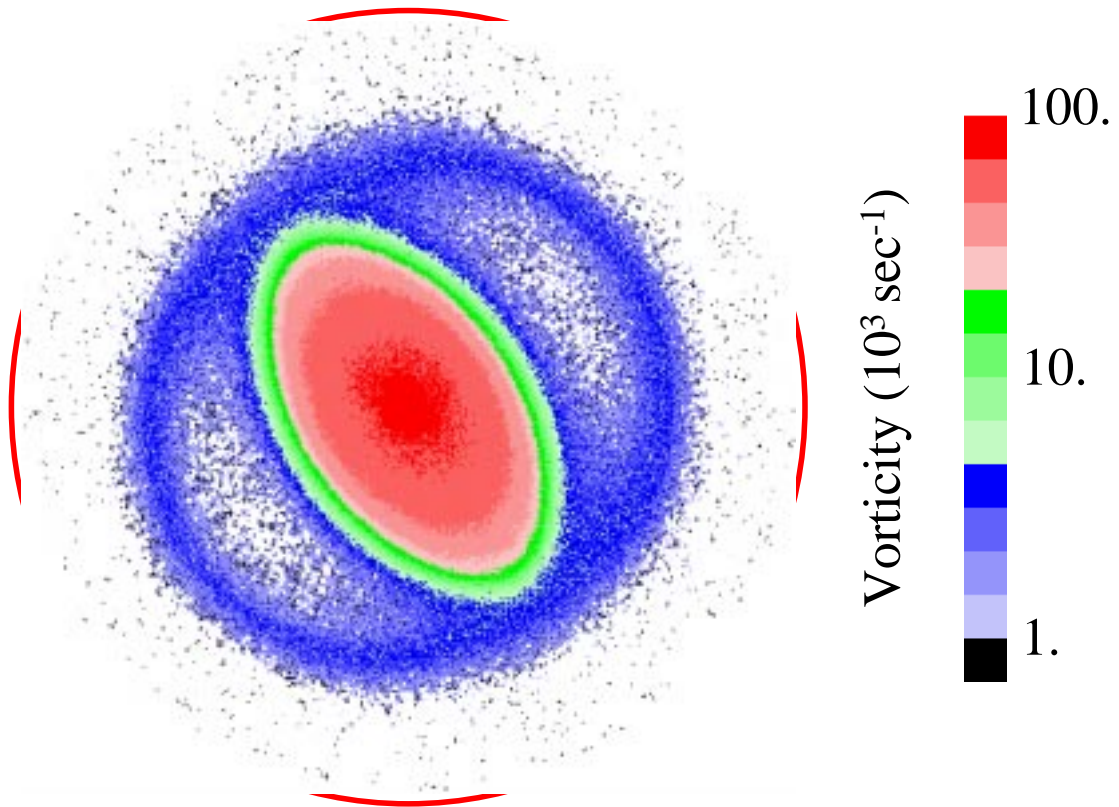
Figure 19. Image of $\zeta(r, \theta)$ after continuously driving the m=2 wave for 50 ms. The nonlinear, long-lived cat's eye flow structures are clearly visible.

K. Eigenmode Analysis

Inviscid wave damping can be understood in the linear amplitude regime by decomposing the vorticity perturbation into independent eigenmodes. In essence, the damped wave is a quasimode consisting of a group of undamped eigenmodes; the observed damping results from a de-phasing of the eigenmodes, each of which propagates at a slightly different frequency.

The theory is simplest for a monotonically decreasing vortex profile $\zeta_0(r)$, i.e.,

$$\frac{d\zeta_0(r)}{dr} \leq 0 \quad \text{for} \quad 0 < r \leq R_W, \tag{22}$$

$$\zeta_0(r) = 0 \quad \text{for} \quad r > R_V.$$

For simplicity, we focus on the discretized eigenmode analysis, wherein the continuous radial variable r is described by a grid $r_j = j\Delta$, with $j = 0,1,\ldots N_W$ and $\Delta = R_W / N_W$. However, for notational clarity we display continuous integrals rather than discretized sums. Each azimuthal Fourier component m is treated separately, and we are interested only in the m=2 component, denoted $\delta\zeta \equiv \delta\zeta^{(2)}$.

The free evolution of an arbitrary initial single-m perturbation can then be decomposed as

$$\delta\zeta(r_j,t) = \sum_{k=1}^{N_v-1} A_k(t)\, \xi_k(r_j)\, e^{-i\omega_k t} + A_d(t)\, \xi_d(r_j) e^{-i\omega_d t}. \tag{23}$$

The sum represents the contribution of the $N_v \equiv R_v / \Delta$ "continuum" modes with frequencies $\omega_k = m\Omega_0(r_k)$ spanning the range of fluid rotation rates from the center to the edge of the vorticity distribution. The second term represents a possible "discrete" mode, with resonant radius outside the vortex. When $\zeta_0(r)$ extends past the critical radius r_c, there is no discrete mode.

Together, these modes form a complete, orthogonal set, with orthogonality relations

$$\langle \xi_k | \xi_{k'} \rangle \equiv \int_0^{R_W} dr\, r^2 (\frac{d\zeta_0}{dr})^{-1} \xi_k(r)\, \xi_{k'}(r) \approx \Delta \sum r_j^{\,2} \left|\frac{d\zeta_0}{dr}\right|_{r_i}^{-1} \xi_k(r_j)\, \xi_{k'}(r_j) = \delta_{kk'}. \tag{24}$$

The modes are solutions of the linearized 2D Euler equations,

$$[\omega - m\Omega_0(r)]\,\xi_k + \frac{m}{r}\frac{d\zeta_0}{dr}\int_0^{R_W} g(r,r')\,\xi_k(r')\,r'\,dr' = 0 \tag{25}$$

where

$$g(r,r') = \frac{1}{m}\left(\frac{r_>}{r_<}\right)\left[1 - \left(\frac{r_>}{R_W}\right)^{2m}\right] \tag{26}$$

is the Green's function for a free-slip circular boundary at $r = R_W$. Note that any physically valid perturbation has $\delta\zeta(r) = 0$ for $r > R_V$, so we need not consider eigenfunctions ξ_k with $N_v < k < N_W$ which are non-zero at any radius $r > R_V$.

Figure 20 shows the eigenvalues and selected eigenfunctions for $\zeta_0(r)$ from Fig. 11, where we observed an undamped wave. Here, $N_W = 400$. The eigenvalues ω_k / m for each of the N_v continuum eigenmodes are plotted as plus signs in Fig. 20 (top); they are seen to overlay the curve of $\Omega_0(r)$. We plot continuum mode eigenfunctions $\xi_k(r)$ for k=45 and k=80 in Fig. 20 (bottom). Note that the continuum eigenfunction consists of positive and negative spikes localized about $r = r_k$ for which $m\Omega_0(r_k) = \omega_k$, with some additional "wings". The discrete eigenvalue, ω_d, representing the observed undamped wave discrete mode, lies outside of the continuum of rotation frequencies $\left[\Omega_0^{\max}, \Omega_0^{\min}\right]$ within the vortex. The discrete mode eigenfunction has an extended radial structure which is closely approximated by $r^{m-1}\,d\zeta_0 / dr$. It is essentially a generalized Kelvin mode on a monotonically decreasing vortex.
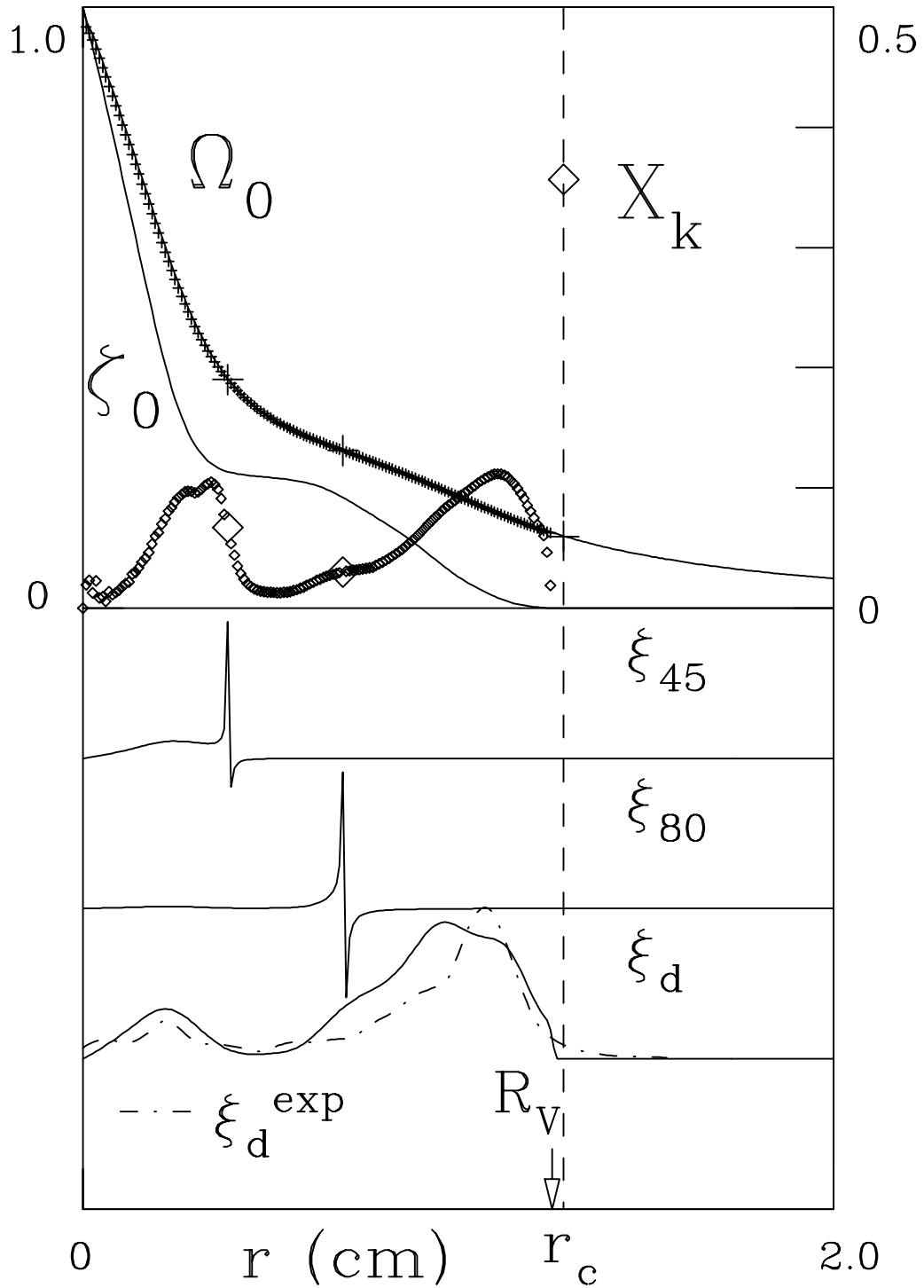
Figure 20. The calculated continuum eigenvalues ω_k / m (crosses); selected eigenfunctions ξ_k (lower curves); measured wave ξ_d^{exp} (dashed); and excitability X_k (diamonds) for the measured vortex of Figs. 11 and 12. $N_W = 400$ and the dashed vertical line marks the critical layer r_c.

The measured wave structure $\xi_d^{\text{exp}}(r)$ is plotted dashed in Figure 20 (bottom), and is well described by the discrete mode predicted from linear theory $\xi_d(r)$. Wave frequencies agree to within the 10% calibration of our phosphor.

Interestingly, we find that wall perturbations excite no significant amount of continuum modes: the contribution from continuum modes in Equation (23) is generally a factor of 10 less (at the level of experimental noise), suggesting that continuum modes do not couple to or cause significant flow perturbations outside the vortex. We characterize the coupling of these modes to outside perturbations by calculating a quantity called the excitability, X_k. The eigenmode excitability is the amplitude to which a mode is excited from our wall perturbation [48]. The excitability coefficient X_k of eigenmode ξ_k is

$$X_k = \left\langle \xi_k \left| r^{m-1} \frac{d\zeta_0}{dr} \right. \right\rangle \tag{27}$$

where $\langle \ \rangle$ indicates the orthogonality integral of Equation (24). In Fig. 20, we plot excitability X_k as diamonds, and find that the discrete mode is predicted to be excited to an amplitude 3 times higher than any continuum mode. In experiments on other vorticity profiles, we have found that the discrete mode typically has excitability 10 times greater than any of the continuum modes. Thus, our experiments and linear eigenmode theory agree that in general, the discrete mode couples strongly to multipole fields outside the vortex, and, once excited, persists indefinitely.

L. Analysis of Damped Quasimodes

The inviscid damping of wave perturbations on vortices where the vorticity is non-zero at the critical radius, such as $\zeta_0(r)$ from Fig. 13, can be understood as the "phase-mixing" of a group of continuum modes. The group of continuum modes will be excited in phase by an external perturbation, and together constitute a "quasimode" which appears to damp exponentially with time.

Figure 21 (top) shows the m=2 eigenvalues ω_k / m calculated for our measured ζ_0. All the eigenfunctions ξ_k with $k > N_v$ are "invalid", in that they have non-zero amplitude where $\zeta_0 = 0$. There is no discrete mode with resonant layer outside the vortex. However, several continuum modes $\xi_k(r)$ are "exceptional" in that they exhibit the extended spatial structure similar to the discrete mode, with added spikes on either side of their resonant radii. In Fig. 21 (bottom) we plot three adjacent exceptional continuum modes, i.e., $k = 150,\ 154$ (marked as "center"), and 165, for $N_W = 400$. The experimentally observed damped quasimode has frequency $f_q = 15\ \text{kHz} = \omega_{\text{cen}} / 2\pi$. The dashed line is the measured quasimode structure $\xi_q^{\text{exp}}(r)$ from Fig.13 (bottom). The measured quasimode agrees well with the extended radial structure of the exceptional continuum modes.

These exceptional continuum modes are also exceptionally strongly excited by external perturbations: the excitability coefficients X_k, plotted in Fig 21 (top) are seen to be a factor of 5 larger than those for non-exceptional continuum modes are. Thus, an external quadrupole flow perturbation will excite this packet of continuum modes,
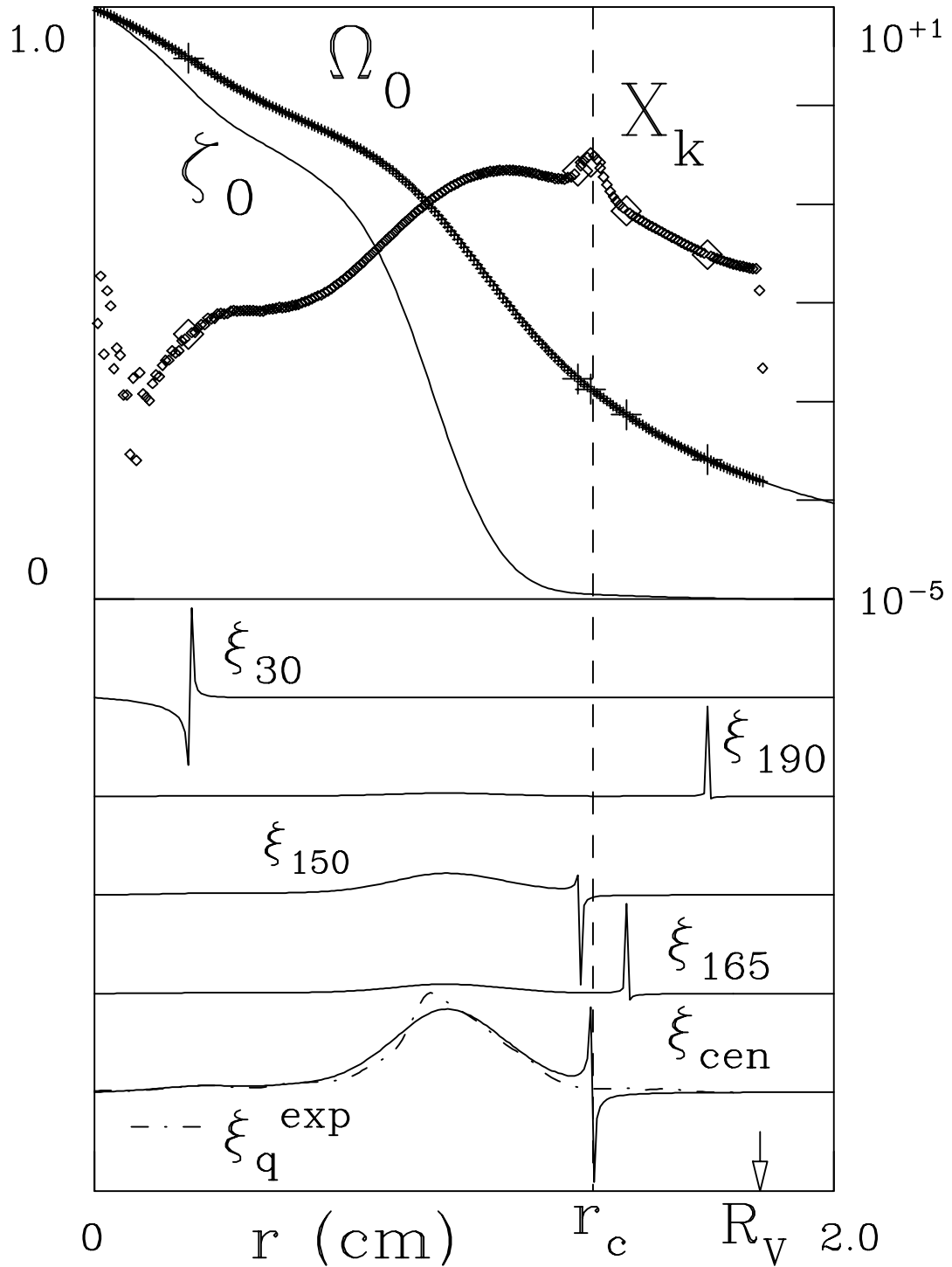
Figure 21. The calculated continuum eigenvalues ω_k / m (plotted as crosses); selected eigenfunctions ξ_k (lower curves); measured quasimode structure ξ_q^{exp} (dashed); and excitability X_k (diamonds) for the measured vortex of Fig. 13. $N_W = 400$ and the dashed vertical line marks the critical layer r_c.

and they will all initially be in phase. Since each continuum mode in this group

propagates at a different frequency, the modes will eventually lose coherence and

destructively interfere. This de-phasing and interference gives the experimentally

observed exponential damping of the quasimode.

In order to obtain a rough estimate of the damping rate, we fit the peak in X as a

Lorentzian of half-width half-max β, as

$$X(r) = \frac{A\beta^2}{(r - r_c)^2 + \beta^2} + Br + C \qquad (28)$$

where β, A, B, and C are parameters to be determined by the fit. One expects

theoretically that the de-phasing will result in an exponential damping rate γ^{th} given

by

$$\frac{\gamma^{th}}{\omega_q} = \frac{\beta}{\Omega_0(r_c)} \frac{d\Omega_0}{dr} . \qquad (29)$$

For the peak of Fig. 21, we obtain $\gamma^{th} / \omega_q \approx 8 \times 10^{-2}$, whereas the observed wave

damping gives $\gamma / \omega_q \approx 3.5 \times 10^{-2}$. Measurements on two other vorticity profiles

$\zeta_0(r)$ gave $\gamma / \gamma^{th} = 0.73$ and 1.5.

An alternate approach to the linear theory, first discussed by Briggs, Daugherty,

and Levy [12], predicts the asymptotic damping of an initial-value perturbation by

analytic continuation in the complex (r, Ω)-plane. In this formulation, it is possible to

find "poles" at frequencies representing exponentially damped quasimodes. We use a

code written by Spencer and Rasband [13] which implements this method of complex

integration, and find that γ^{BDL} / ω_q agrees with our measured γ / ω_q to within a factor of 0.2-1.8.

Finally, we note that several different exceptional waves can exists on vorticity profiles with more than one distinct "edge." The existence of multiple m waves was first suggested by Rayleigh [53], for piecewise continuous $\zeta_0(r)$, in which one wave occurs per distinct ζ_0 piece. Our experimental $\zeta_0(r)$, shown in Fig. 13, is much smoother than Rayleigh's, but still possesses several distinct "shoulders," including an inner slope centered around $r = 0.8$ cm and an outer slope at $r = 1.4$ cm. Sinusoidal wall voltages at $f = 20$ kHz excite a quasimode ξ_{inner} on the inner slope with frequency $f_{inner} = 21.5$ kHz and a quasimode on both inner and outer slopes, ξ_{outer}, with frequency $f_{outer} = 12.5$ kHz. Here again, the observed damped waves have spatial structure given by the $\xi_k(r)$ of "exceptional" continuum modes. When the damping is weak due to small $d\zeta_0 / dr \big|_{r_c}$, the quasimodes may persist and be detected in experiments; for strong damping, the continuum modes phase-mix rapidly and no wave is detected in practice.

REFERENCES

1. Frisch, U. and S.A. Orszag, *Turbulence: challenges for theory and experiment.* Physics Today, 1990. **43**(1): p. 24-32.

2. Surko, C.M. and R.E. Slusher, *Waves and turbulence in a Tokamak fusion plasma.* Science, 1983. **221**(4613): p. 817-22.

3. Nelkin, M., *In what sense is turbulence an unsolved problem?* Science, 1992. **255**(5044): p. 566-70.

4. Pedlosky, J., *Geophysical fluid dynamics*. 2nd ed. 1987, New York: Springer-Verlag. xiv, 710.

5. Krall, N.A. and A.W. Trivelpiece, *Principles of plasma physics*. International series in pure and applied physics. 1973, New York,: McGraw-Hill. xiii, 674.

6. Kraichnan, R.H. and D. Montgomery, *Two-dimensional turbulence.* Reports on Progress in Physics, 1980. **43**(5): p. 547-619.

7. Roshko, A., *Structure of turbulent shear flows: a new look.* AIAA Journal, 1976. **14**(10): p. 1349-57.

8. Tabeling, P., *et al.*, *Experimental study of freely decaying two-dimensional turbulence.* Physical Review Letters, 1991. **67**(27): p. 3772-5.

9. Driscoll, C.F., J.H. Malmberg, and K.S. Fine, *Observation of transport to thermal equilibrium in pure electron plasmas.* Physical Review Letters, 1988. **60**(13): p. 1290-3.

10. Peurrung, A.J. and J. Fajans, *A limitation to the analogy between pure electron plasmas and two-dimensional inviscid fluids.* Physics of Fluids B (Plasma Physics), 1993. **5**(12): p. 4295-8.

11. Fine, K.S., *et al.*, *Relaxation of 2D turbulence to vortex crystals.* Physical Review Letters, 1995. **75**(18): p. 3277-80.

12. Briggs, R.J., J.D. Daugherty, and R.H. Levy, *Role of Landau damping in crossed-field electron beams and inviscid shear flow.* Physics of Fluids, 1970. **13**(2): p. 421-32.

13. Spencer, R.L. and S.N. Rasband, *Damped diocotron quasi-modes of non-neutral plasmas and inviscid fluids.* Physics of Plasmas, 1997. **4**(1): p. 53-60.

14. Malmberg, J.H. and J.S. de Grassie, *Properties of nonneutral plasma.* Physical Review Letters, 1975. **35**(9): p. 577-80.

15. Driscoll, C.F. and J.H. Malmberg, *Hollow electron column from an equipotential cathode.* Physics of Fluids, 1976. **19**(5): p. 760-1.

16. Driscoll, C.F. and K.S. Fine. *Experiments on vortex dynamics in pure electron plasmas.* 1990.

17. Levy, R.H., *Diocotron Instability in a Cylindrical Geometry.* Physics of Fluids, 1965. **8**: p. 1288-1295.

18. Levy, R.H., *Two New Results in Cylindrical Diocotron Theory.* Physics of Fluids, 1968. **11**: p. 920-21.

19. Kraichnan, R.H., *Inertial ranges in two-dimensional turbulence.* Physics of Fluids, 1967. **10**: p. 1417.

20. Batchelor, G.K., *Computation of the energy spectrum in homogeneous two-dimensional turbulence.* Physics of Fluids, 1969: p. II 233-9.

21. Onsager, L., *Statistical Hydrodynamics.* Nuovo Cimento Suppl., 1949. **6**: p. 279.

22. Joyce, G. and D. Montgomery, *Negative temperature states for the two-dimensional guiding-centre plasma.* Journal of Plasma Physics, 1973. **10**(pt.1): p. 107-21.

23. Bretherton, F.P. and D.B. Haidvogel, *Two-dimensional turbulence above topography.* Journal of Fluid Mechanics, 1976. **78**(pt.1): p. 129-54.

24. Leith, C.E., *Minimum enstrophy vortices.* Physics of Fluids, 1984. **27**(6): p. 1388-95.

25. Huang, X.P. and C.F. Driscoll, *Relaxation of 2D turbulence to a metaequilibrium near the minimum enstrophy state.* Physical Review Letters, 1994. **72**(14): p. 2187-90.

26. Smith, L.M. and V. Yakhot, *Bose condensation and small-scale structure generation in a random force driven 2D turbulence.* Physical Review Letters, 1993. **71**(3): p. 352-5.

27. McWilliams, J.C., *The emergence of isolated coherent vortices in turbulent flow.* Journal of Fluid Mechanics, 1984. **146**: p. 21-43.

28. Carnevale, G.F., *et al.*, *Evolution of vortex statistics in two-dimensional turbulence.* Physical Review Letters, 1991. **66**(21): p. 2735-7.

29. Weiss, J.B. and J.C. McWilliams, *Temporal scaling behavior of decaying two-dimensional turbulence.* Physics of Fluids A (Fluid Dynamics), 1993. **5**(3): p. 608-21.

30. Benzi, R., *et al.*, *A simple point vortex model for two-dimensional decaying turbulence.* Physics of Fluids A (Fluid Dynamics), 1992. **4**(5): p. 1036-9.

31. Dritschel, D.G., *Vortex properties of two-dimensional turbulence.* Physics of Fluids A (Fluid Dynamics), 1993. **5**(4): p. 984-97.

32. Cardoso, O., D. Marteau, and P. Tabeling, *Quantitative experimental study of the free decay of quasi-two-dimensional turbulence.* Physical Review E (Statistical Physics, Plasmas, Fluids, and Related Interdisciplinary Topics), 1994. **49**(1): p. 454-61.

33. Yarmchuk, E.J., M.J.V. Gordon, and R.E. Packard, *Observation of stationary vortex arrays in rotating superfluid helium (TV observation technique).* Physical Review Letters, 1979. **43**(3): p. 214-17.

34. Campbell, L.J. and R.M. Ziff, *Vortex patterns and energies in a rotating superfluid.* Physical Review B (Condensed Matter), 1979. **20**(5): p. 1886-902.

35. Mitchell, T.B. and C.F. Driscoll, *Symmetrization of 2D vortices by beat-wave damping (electron coloumns).* Physical Review Letters, 1994. **73**(16): p. 2196-9.

36. Pillai, N.S. and R.W. Gould, *Damping and trapping in 2D inviscid fluids.* Physical Review Letters, 1994. **73**(21): p. 2849-52.

37. McWilliams, J.C., *The vortices of two-dimensional turbulence.* Journal of Fluid Mechanics, 1990. **219**: p. 361-85.

38. Schecter, D.A. and D.H.E. Dubin, *Motion of a Single Vortex Through Shear-Flow.* Bull. Am. Phys. Soc., 1996. **42**(7): p. 1604.

39. Schecter, D.A. and D.H.E. Dubin, *Vortex Crystals: Experiment and Simulation.* in press.

40. Huang, X.P., K.S. Fine, and C.F. Driscoll, *Coherent vorticity holes from 2D turbulence decaying in a background shear flow.* Physical Review Letters, 1995. **74**(22): p. 4424-7.

41. Jin, D.Z. and D.H.E. Dubin, *Regional Maximum Entropy Theory of Vortex Crystals.* in press.

42. Mitchell, T.B., C.F. Driscoll, and K.S. Fine, *Experiments on stability of equilibria of two vortices in a cylindrical trap.* Physical Review Letters, 1993. **71**(9): p. 1371-4.

43. Kelvin, W., *Vibrations of a columnar vortex.* Phil. Mag., 1880. **10**: p. 155-168.

44. Deem, G.S. and N.J. Zabusky, *Vortex waves: Stationary 'V states', interactions, recurrence, and breaking.* Physical Review Letters, 1978. **40**(13): p. 859-62.

45. de Grassie, J.S. and J.H. Malmberg, *Wave-induced transport in the pure electron plasma.* Physical Review Letters, 1977. **39**(17): p. 1077-80.

46. Brown, S.N. and K. Stewartson, *On the algebraic decay of disturbances in a stratified linear shear flow.* Journal of Fluid Mechanics, 1980. **100**(pt.4): p. 811-16.

47. Corngold, N.R. *Linear response of the 2-d pure electron plasma; quasi-modes for model profiles.* 1995.

48. Schecter, D.A. and D.H.E. Dubin, in preparation.

49. Davidson, R.C., *Theory of nonneutral plasmas.* Frontiers in physics no. 43. 1974, Reading, Mass.,: W. A. Benjamin. xiii, 199.

50. Kelvin, W., *On a Disturbing Infinity in Lord Rayleigh's Solution for Waves in a Plane Vortex Stratum.* Nature, 1880. **23**: p. 45-46.

51. Bernoff, A.J. and J.F. Lingevitch, *Rapid relaxation of an axisymmetric vortex.* Physics of Fluids, 1994. **6**(11): p. 3717-3723.

52. Koumoutsakos, P., *Inviscid axisymmetrization of an elliptical vortex.* Journal of Computational Physics, 1997. **138**(2): p. 821-57.

53. Rayleigh, J.W.S., Proc. London Math. Soc., 1880. **11**: p. 57.